Observations of high-frequency internal waves in the Coastal Ocean Dynamics Region

James M. Pringle[1]

Woods Hole Oceanographic Institution, Woods Hole, Massachusetts, 02543

Abstract. Current meter data from the second Coastal Ocean Dynamics Experiment (CODE II) for July 1982 are analyzed for internal waves in the 6 to 40 cycles per day (cpd) frequency band. It is found that the wave field is anisotropic and that the current ellipses are oriented in approximately the cross-isobath direction. The squares of the ratio of the major to minor axes of the current ellipses (the "ellipticity") are consistent with a continuum of internal waves propagating onshore but are not consistent with a single wave propagating onshore. The reduction of internal wave energy across the shelf is consistent with propagation from the deep ocean or shelf break, as is the correlation between vertical velocities and velocities parallel to the minor axis. However, there is evidence for the generation of additional internal wave energy on the shelf in the evolution of the current ellipses across the shelf and in the bluing of the internal wave spectra across the shelf. Internal wave energy levels are elevated by a factor of 1.5 to 5 above *Garrett and Munk* [1972] levels at the moorings on the 130 and 365 m isobaths. The first vertical mode dominates at the 130 m isobath, the only mooring for which the vertical modal analysis was done.

1. Introduction

In the deep ocean, away from horizontal and vertical boundaries, the high-frequency internal wave spectrum is well modeled by the *Garrett and Munk* [1972] spectrum (hereafter referred to as GM). In shallow coastal regions there is no such universal description of the internal wave field. Thus it is useful and interesting to examine the internal wave climate at a particular shelf location. The current meters and thermistors deployed during the Coastal Ocean Dynamics Experiment (CODE) allow one to examine how the high-frequency internal wave spectrum changes across a continental shelf. This is done for the central current meter array of the CODE II experiment for the month of July 1982. An accompanying study by *Pringle and Brink* [this issue] (hereafter referred to as PB) models linear internal wave propagation from the shelf break to the coast using a GM spectrum as the deep ocean initial condition. To the extent that the observations and theory can be compared and differ, it gives an idea of how much of the internal wave energy on the shelf is generated on the shelf and how much propagates in from the ocean. A detailed comparison of PB and the data is impossible because the data are unable to resolve the horizontal wave number spectrum of the internal waves,

and the internal wave spectrum in the ocean adjacent to the shelf is also unknown.

For the CODE region, high-frequency waves have been defined, somewhat arbitrarily, as those with frequencies between 6 and 40 cycles per day. This range of frequencies is between the highest frequency of critical topographical reflection of internal waves (6 cpd) and the lowest buoyancy frequency observed on the shelf for the time of the analysis (40 cpd). The month of July 1982 was chosen because the stratification was relatively constant throughout the month and the hydrographic structure was generally simple. The same analysis as presented herein can be performed for other times in the data record. The results do not seem qualitatively different, but the analysis is difficult because of the uncertainties in calculating the stratification at the current meters in other months.

The high-frequency internal wave climate on the shelf is interesting, not only in its own right but also because it can affect diapycnal mixing [*Sandstrom and Elliott*, 1984; *Sanford and Grant*, 1987] and the propagation of acoustic energy on the shelf [*Lynch et al.*, 1996]. It has been studied by several authors, including *Gordon* [1978], who analyzed internal waves using current meter data taken off Spanish Sahara at 21°N, 17°W as part of the 1974 JOINT-1 experiment. That shelf has a bottom slope, 2×10^{-3}, between those typical of the east and west coasts of North America. Gordon concluded from an empirical orthogonal function analysis that most of the energy is in the first-mode internal waves and that those waves propagated toward the shore. He claimed that energy dissipation was dominated by the effects of shoaling as the waves entered shallow water and by the subsequent nonlinear dissipative effects of wave breaking.

Another analysis of internal wave data by *Howell and Brown* [1985] is of interest because it was done at the same site as the present analysis. Howell and Brown analyzed six internal wave soliton events that occurred during a six day period in April 1981. They conclude that they did observe solitons with a period of about 25 minutes, and that the events corresponded well with two-layer soliton theory. Howell and Brown's conclusions would have to be included in any more complete analysis of internal waves on the shelf.

2. Internal Wave Background

Garrett and Munk [1972] codified the deep water internal wave spectrum, and their scheme has proven to be surprisingly robust away from horizontal boundaries, vertical boundaries, and the equator [*Wunsch*, 1976].

There is no reason to expect that it will be correct on or near the shelf. However, since deep ocean internal waves may propagate onto the shelf and since whatever processes maintain the deep ocean at the GM spectrum may also drive the coastal internal wave spectrum locally, the GM spectrum makes a useful point of reference for any observed spectrum. In PB the propagation of a GM spectrum onto the shelf is explicitly modeled, but whatever nonlinear processes equilibrate the GM spectrum in the deep ocean are not considered.

The GM spectral power density is, for horizontal currents observed by a current meter that moves with the subinertial current,

$$\left\langle u^2 \right\rangle + \left\langle v^2 \right\rangle = (4Eb^2N_0)Nf\omega^{-3}\frac{\omega^2+f^2}{\sqrt{\omega^2-f^2}}, \qquad (1)$$

where $(4Eb^2N_0)$ is a scale power spectral density of 2.2 m^2s^{-1}; $\left\langle u^2 \right\rangle$ and $\left\langle v^2 \right\rangle$ are the volume-averaged horizontal current variances; and N, f, and ω are the local buoyancy, inertial, and internal wave frequencies, respectively. When $\omega^2 \gg f^2$, the power spectrum can be simplified to

$$\left\langle u^2 \right\rangle + \left\langle v^2 \right\rangle = (4Eb^2N_0)Nf\omega^{-2} \qquad (2)$$

with very little error.

Wunsch [1968,1969] and *McKee* [1973] examined internal waves propagating in a uniformly stratified wedge. The McKee solutions show that incoming internal wave crests turn to parallel the beach in the same way that surface gravity waves do. They also derive the slope c for critical internal wave reflection off the bottom:

$$c = \sqrt{\frac{\omega^2-f^2}{N^2-\omega^2}} \qquad (3)$$

If the bottom slope is steeper than c, the wave will be reflected back to deeper water. If the slope is less than $0.5c$, the bottom appears locally flat, and if the slope is nearly equal to c, a region of strong shear will exist near the bottom.

3. Topography and Coordinates

The CODE region, which is described by *Beardsley and Lentz* [1987], is centered around 123°30W and 38°30N, between Point Arena and Point Reyes, California. Figure 1 shows the location of the current meter moorings used in the present analysis. The coastline is straight for about 75 km, the straight portion being approximately centered on the central ("C") moorings. The alongshore and cross-shelf directions are defined

Figure 1

by the mean orientation of the coast around the central array; the cross-shore axis points to 47°T, and the alongshore axis points to 317°T. [*Beardsley et al.*, 1985]. The shelf break, however, is not parallel to the shore. A coordinate system defined by the 365 m isobath is rotated by about 17° clockwise from the coordinate system defined at the shelf.

The shelf break is at about 200 m, and the slope of the shelf averages 5×10^{-3} between C4 and C3 (130 and 90 m depth, respectively) and 5×10^{-2} at C5. C5 is in 365 m of water, beyond the shelf break at 200 m.

Wunsch [1969] solves for the characteristic slope of an internal wave. If the bottom slope is greater than the characteristic slope of an internal wave, the wave can no longer be represented with vertical modes and internal wave energy reflecting off the bottom will be sent back to the deep sea (PB). Since much of the analysis here considers the propagation of internal waves from the deep ocean onto the shelf, the analysis will be restricted to frequencies whose characteristic slope is everywhere greater than the bottom slope. This is true when

$$\omega > \sqrt{\frac{f^2 + \alpha^2 N^2}{1 + \alpha^2}} \approx \sqrt{f^2 + \alpha^2 N^2}, \qquad (4)$$

where α is the bottom slope. An N of 100 cpd, an f of 1.24 cpd, and a maximum bottom slope on the shelf break of 6×10^{-2} restricts the analysis to frequencies greater then 6 cycles per day. This also avoids internal waves at the tidal and inertial frequencies, whose forcing mechanisms are likely to be different than the forcing mechanisms of the higher-frequency internal waves. The critical frequency on the shelf, with its slope of 5×10^{-3}, is only 5% higher than f, and so is not near the frequencies analyzed here.

4. Hydrography

The month of July 1982 was chosen for analysis because the hydrography had a simple relationship between temperature and density, which allows the calculation of density σ from the temperatures T observed at the current meters. The overall hydrography is typified by Figure 2, an average for the April to July upwelling season (Figure 2 is drafted from *Kosro and Huyer* [1986, Figure 24]). It is similar to the two sections taken on July 16 and 19, 1982, and the many other conductivity-temperature-depth (CTD) casts taken in July [*Huyer et al.*, 1983].

Figure 2

A relation between temperature and potential density was formed from the CTD casts taken during July in the CODE region on the shelf and shelf break. Only data

from less than 400 m were used to obtain the relation

$$\sigma = -0.1781T + 27 \qquad T < 7.74°\text{C} \tag{5a}$$
$$\sigma = -0.2633T + 28 \quad 7.74°C < T < 9.212°\text{C} \tag{5b}$$
$$\sigma = -0.1975T + 28 \qquad T > 9.212°\text{C} \tag{5c}$$

This includes both the effect of the nonlinearity of the equation of state and the observed T/S relation. The RMS difference between (5) and the density computed with the full equation of state is 0.085 kg m^{-3}. To provide confidence in this empirical relation, the buoyancy frequency from the CTD sections is plotted as computed from the full equations of state and as computed from (5a)-(5c) (Figure 3). Though not a rigorous test, since it uses the same data as used to derive the σ/T relation, it is reassuring that there are few outliers. This σ/T relation allows one to compute densities from the temperature records at each current meter. A representative middepth time series of N^2 is shown for the water between 55 and 70 m at the C4 mooring in Figure 4. The temperature data used for Figure 4 were low-pass filtered with a half-amplitude pass at 3.25 times the inertial period (f=1.24 cpd) and a full-amplitude pass at 4 times the inertial period. This removes the displacements in the density field caused by the internal waves.

Figure 3

Figure 4

5. Low-Frequency Currents

Unfortunately, the high-frequency data needed to study internal waves were only archived for the moorings at the 130 and 365 m isobaths. There are only hourly data available for the moorings shoreward of 130 m. Thus most of the following analysis can only be done with the C5 mooring in 365 m of water and the C4 mooring in 130 m of water. The C4 mooring had usable current meters at 10 and 20 m on a surface mooring and at 35, 55, 70, 90 and 121 m on a subsurface mooring 100 m away. The C5 mooring had instruments at 20, 35, 55, 70, 90, 110, 150, 250, and 350 m [*Beardsley et al.*, 1985].

The alongshore subinertial currents during July had two main characteristics. At the 90 m (C3) and 365 m (C5) moorings, alongshore flow was equatorward ($v \approx -5$ to -15 cm s^{-1}) for the first 15 days of the month and poleward the next 16 days ($v \approx 5$ to 15 cm s^{-1}). This was also true of the alongshore currents at 90 m and below at the 130 m (C4) mooring. However, the currents were persistently equatorward in the water above 90 m at C4. The cross-shelf currents were less vigorous than the alongshore currents. The barotropic current at C4 is equatorward for the first 15 days and nearly zero for the next 15 days. Figure 5 shows plots of

Figure 5

representative alongshore currents at C3, C4, and C5. For more information on the low-frequency currents, see *Winant et al.* [1987].

6. Analysis at Individual Current Meters

The GM model makes three strong statements about the internal wave spectrum in the deep ocean. The shape of the power spectrum of horizontal currents goes roughly as ω^{-2}, the energy level is fixed, and the spectrum is isotropic. However, it will be shown below that the shape of the internal wave spectrum on the shelf varies across the shelf, the internal wave energy levels vary with mooring and time, and the spectra are never isotropic.

Figure 6 shows power spectra of velocity from the C5, C4, and C3 moorings, at depths chosen because they illustrate well the general trends of the spectra. The power spectra are computed with half-overlapped Welsh windows of period $4\pi/f$, so that the spectra resolve the full internal wave band including tidal and inertial frequencies (though these peaks are not prominent in the data). The spectra become less red as one moves onshore, the energy levels decrease, and the current ellipses are not the circles that GM predicts for the deep ocean. In section 7 it will be shown with energy arguments that the high-frequency data are consistent with internal waves.

Figure 6

6.1. Horizontal Current Kinetic Energy

The total mean square current, u^2+v^2, in the 6 to 40 cpd wave band is plotted for current meters C4 and C5 in Figure 7. The mean square current has been scaled by the GM spectrum for the time-averaged buoyancy frequency, so a value of 1 would match the kinetic energy in the GM spectrum. The power at both locations is consistently larger than the GM power. The power at the C5 mooring is greater than at the C4 mooring, both when integrated over the water column and averaged over the water column. The depth-averaged power is reduced by a factor of about 1.5 between C5 and C4, while the depth-integrated power is reduced by about 4, which is consistent with the frictional dissipation of shoreward propagating internal waves as described by *Brink* [1988] and modeled in PB, and it strongly supports the idea that most of the internal wave energy on the shelf is propagating in from the deep ocean or shelf break and being dissipated as it moves shoreward. If energy were propagating adiabatically from offshore, both the power integrated over the water column and

Figure 7

the power per vertical distance should increase toward the shore as the waves shoal (PB). If the waves were propagating from the coast outward, the power should likewise increase shoreward, with or without friction, because both friction and shoaling work to reduce the energy in the wave as it moves offshore. Thus the reduction of internal wave power as one moves closer to the shore is a robust indication that energy is propagating from the deep ocean or shelf break and is being dissipated as it moves to the shore. The limited amount of data at the 90 m C3 mooring (Figure 6) indicates that the internal wave energy continues to decay across the coast, again consistent with PB.

The enhanced energy near the surface and the bottom at C4 suggests that the internal waves there are dominated by the first baroclinic mode, which is consistent with the modal analysis presented below. The lack of a similar enhancement at C5 argues that mode 1 is not dominant in the deeper water.

6.2. Spectral Shape

In Figure 6 one can see that the log-log spectral slope becomes less steep as one moves toward the shore. This is confirmed by Figure 8, which shows the spectral slopes at all the current meters on the 365 m and 130 m moorings. The slope is computed from a linear least squares fit between the log of the power and the log of the frequencies analyzed. There were not enough spectral data to analyze robustly the power laws at the C3 site. The slopes at the 365 m mooring are around 1.8, except for the deepest current meter, where the slope is steeper. The slopes for the 130 m mooring cluster around 1.5. Since the 1 standard deviation uncertainty of the fits is less than 0.06, these slopes are significantly different. The reduction of the slope of the shallow water spectra is puzzling if one views the internal waves as propagating in from the deep sea. Since the waves decay at a roughly constant rate per unit time [*Brink*, 1988; *Sanford and Grant*, 1987; PB], one would expect the high-frequency waves, which are slower, to be dissipated more strongly per unit distance as they move onshore. This would redden the spectrum by selectively dissipating the higher-frequency waves. The resolution of this discrepancy may lie in a conjectural nonlinear interaction that transfers energy from low-frequency waves to higher-frequency waves or in the preferential generation of high-frequency internal waves on the shelf or shelf break. For instance, the high-frequency internal solitons found by *Howell and Brown* [1985] could, if generated between the 365 m and 130 m site, account for some of the extra high frequency energy. The relative

Figure 8

excess of high-frequency energy over low is the greatest disagreement between PB and the data.

6.3. Lack of Isotropy: Predictions From PB

The GM spectrum is isotropic, but it is no surprise that the internal wave spectrum has a strong polarization near the coast. *McKee* [1973] studied internal waves propagating into a wedge-shaped topography. He noted that internal wave crests turn to parallel the coast as surface gravity waves do. This tends to focus the wave energy toward the coast.

If the internal waves start at the shelf break with no preferred orientation, those that propagate toward the coast turn, so that their crests become more parallel to the coast. Since internal waves have current ellipses whose major axes are oriented in the direction the waves are propagating, this turning toward the coast tends to make the current ellipses perpendicular to the local bathymetry.

If the waves are generated near the shore and radiate outward, their orientation depends sensitively on the source location and the orientation of the waves generated at the source. Since current ellipses are symmetric around their major and minor axes, the shape of the ellipse does not indicate whether a wave is coming on or offshore. Waves that are generated at the shore but radiate at an angle to the shore will be trapped shoreward of a depth that decreases as the magnitude of the angle to the normal of the shore increases. The ellipse orientation of a trapped wave depends sensitively on the trapping depth and varies as the wave crosses the shelf, and so it depends sensitively on the source geometry.

A mean flow can also alter the internal wave geometry. There are many possible effects. Current shear alters the local relative vorticity and hence the apparent f [*Kunze*, 1985]. The internal wave can trade energy back and forth with the mean current [*Lighthill*, 1978]. The effect that is found in PB to be dominant at these frequencies and for realistic mean currents is the effect of Doppler shifting a red spectrum. A current will Doppler shift the observed wave, so waves traveling with the mean current will be observed at frequencies higher than their intrinsic frequency, and those traveling against the current will be observed at lower than their intrinsic frequency. If the spectrum of the internal waves in the reference frame of the mean current is red, as it almost certainly is, then the amplitude of the waves traveling with the current, which have lower intrinsic frequencies, will be greater. Because of this, the current ellipse will be shifted in the direction of the current.

All of these effects operate at the same time, so distinguishing the relative contributions of each in the data is hard. PB presents a model of these effects for waves of a GM spectrum at the shelf break propagating over the shelf. The model uses ray tracing to follow the horizontal path of internal wave vertical modes and assumes that near the shelf break the path of the internal waves becomes controlled by the bathymetry. This naive treatment of the shelf break, as well as the lack of any alongshore variation in currents and the disregard of any nonlinear effects other than wave interaction with a mean flow, are the primary weaknesses of the model. However, its simplicity has the advantage that its predictions can be easily summarized as follows: (1) Topographic refraction makes the major axis of the current ellipses perpendicular to the isobaths. (2) The ellipticity of the current ellipse, which is the ratio of the horizontal current power in the major axis direction to the power in the minor axis direction, will increase closer to shore but will not depend strongly on wave frequency. Currents of the magnitude seen in the CODE region will not greatly change the ellipticity. (3) The current will tend to shift the major axis of the current ellipse downstream, that is for a positive mean current the angle of the major axis to the cross-shore direction is positive (see Figure 9). For a bathymetry such as that in the CODE region, the mean currents will shift the major axis of the current ellipse of vertical mode 1 and mode 2 waves by only 5 to 15°away from the cross-isobath direction for mean currents less than 20 cm s^{-1}.

Figure 9

In order to disentangle the effects of topography and alongshore current in the data, two types of analysis will be performed. First, the ellipticity and orientation of the currents as a function of frequency for each current meter will be analyzed for two time subperiods, one for when the mean currents were predominantly poleward, one for when they were predominantly equatorward. Then, since the predictions of the effects of the alongshore current depend on the vertical mode structure of the wave, a similar analysis will be done on the the modally decomposed data. It is also with this decomposition that the direction of propagation of the waves can be determined, and the power in the vertical and horizontal currents can be compared to internal wave theory.

6.4. Ellipticity

One observable that indicates anisotropy is the square of the ratio of the major to minor axis of the current ellipse (the "ellipticity"). This is the ratio of the powers

in the horizontal currents in a coordinate system aligned with the major axis. For a single plane wave it varies with frequency as ω^2/f^2. For an isotropic spectrum on an f plane, it is, of course, 1. The theory in PB predicts that the ellipticity of a continuum of waves over the shelf should not be a function of vertical mode and only a weak function of ω and mean currents, until near the coast when all the waves have been topographically refracted to be nearly perpendicular to the coast or until the mean alongshore currents become strong enough to absorb or reflect the waves, neither of which occurs at the C4 or C5 sites.

In order to collapse the data at each current meter in each subperiod into a single number, the ellipticity is calculated for each frequency between 6 and 40 cpd, and those ellipticities are averaged with a constant weighting, ignoring the differences in energy at each frequency. Since the spectra are red, any power-weighted average is approximately the ellipticity at 6 cpd and thus not much more useful than only examining the ellipticity at 6 cpd. The averages are therefore made without power weighting in order to increase the robustness of the statistical tests applied to the averages. Averaging the ellipticity over a range of frequencies is a sensible thing to do for a random isotropic wave spectrum, for each frequency is an independent sample. However, averaging the observed ellipticity over a range of frequencies is still troublesome, for any nonlinear interaction between the waves could introduce correlations between measurements made at different frequencies. Nonetheless, there is no consistent variation of ellipticity with frequency for various current meters, an observation that agrees with the result in PB that ellipticity should be a weak function of ω. This can be seen in the spectra in Figures 6 and 10, in which there are no consistent variations in the ratio of the power spectra of the cross-shore and alongshore velocity in the 6 to 40 cpd frequency range.

As an observed quantity, ellipticity is difficult to analyze, for any random time series of currents will have an ellipticity of 1 or greater. Thus the sample average ellipticity of an observed isotropic spectrum will be greater than 1, even though the expected average will asymptote to 1 as the length of the record increases. However, for this analysis the ellipticity at a given frequency is different from an isotropic spectrum with 80% confidence if its ellipticity is greater then 1.37, and the average ellipticity over the 6 to 40 cpd frequency band considered here is different from an isotropic spectrum at the 95% level if the ellipticity is greater then 1.37. That both significance levels are 1.37 is a coincidence.

These significance levels were found by a Monte Carlo technique: the distributions of ellipticity from 10^5 synthetic isotropic time series was computed, and from this the confidence levels were obtained.

Only one of the 32 estimates of the average ellipticity of the data in Table 1 fails to be different from white noise at 95% confidence, so the data must be considered anisotropic. The average ellipticities in Table 1 lie between 2.8 and 1.4, except for the bottommost current meter at C4, whose ellipticity is ≈ 4.75 for the whole record. At C4 the ellipticities are enhanced near the top and bottom to levels that are near the levels that will be obtained for the mode 1 waves in the modal decomposition below. This is consistent with the idea that the internal wave energy at C4 is dominated by mode 1 and suggests that this is not true for C5. None of the current records has ellipticities near the $\omega^2 f^{-2}$ predicted for a single internal wave, so the internal wave field cannot be made up of a single wave propagating in from the shelf break, but the results are consistent with an ensemble of internal waves propagating across the shelf.

Table 1

PB predicts that if all of the internal waves on the shelf had originated as an isotropic wave field in the deep ocean, the ellipticity of the current ellipses should increase as the waves move toward the coast. This is not observed, again suggesting that there is wave generation or modification on the shelf. Waves generated on the shelf would also tend to be turned toward the coast by the topography and thus become consistent with the PB picture closer to shore. A more detailed comparison to the model in PB is not practical, for there is not enough information in the current meter records to compute the horizontal wave number spectra at the current meter moorings, and thus it is impossible to compensate for the naivete of PB's internal wave boundary conditions at the shelf break or to diagnose what waves are generated on the shelf or at the shelf break between C5 and C4.

Interestingly, 13 out of 16 current meters at C5 and C4 had greater ellipticities in the second half of the month, when the water was flowing poleward or less equatorward. The PB model does not predict this effect, which may be caused by alongshore variation in the mean flow or localized generation of internal waves on the shelf or shelf break.

6.5. Current Ellipse Orientation

From the angle of the major axis of the current ellipse to the cross-shore direction, one can get a good constraint on the direction of propagation of energy since

the current ellipse, horizontal wave vector, and intrinsic group velocity are parallel for a single wave. The mean current will Doppler shift the frequency but not change the current ellipse angle of a single wave. However, the orientation of the major axis is ambiguous to the direction of wave propagation by 180°, so the final determination of the direction of energy propagation must use other methods, such as the evolution of cross-shelf power presented above or the correlation between velocities presented later.

The orientation of the major axis of the current ellipse is the angle the major axis makes to the cross-shore direction. The angle is constrained to be between -90° and 90° and is defined in Figure 9 as being positive in the counterclockwise sense.

Figure 10 includes plots of the ellipse orientation for the 55 m current meter at the C5 mooring. It illustrates a surprisingly constant major axis angle over the 6-40 cpd range of the analysis. The scatter of the angles in Figure 10 is smaller than in most other records, but none of the other records shows a trend in the ellipse orientation with frequency. Since the observed angles show no consistent relation to frequency, they have been averaged over the usual range of frequencies. The averages are in Table 1. The significance estimate was again formed with a Monte Carlo technique, in which 10^5 synthetic isotropic random time series were created, and ellipse orientations as a function of frequency were formed as with the data. The mean angle was defined as the angle that is closest to all the angles in a least squared distance sense. Angular distance was defined as being between $-\pi/2$ and $\pi/2$ because ellipse angle is ambiguous to a π radian rotation. The standard deviation of angles around this mean was found for each synthetic isotropic series, and a distribution of these standard deviations was found. The standard deviation of the angles in the data was then compared to the distributions of the synthetic data. All but one of the current meter records have angles whose distributions are significantly (>95% confidence) different from an isotropic wave field. This again shows that the wave field must be considered anisotropic

Several conclusions can be drawn from the angles in Table 1. Thirty-one of 32 averaged angles are negative, and many are near the -17° value consistent with bathymetric steering and, thus are consistent with linear internal wave energy propagating to the shore. (The shelf break is rotated relative to the shore by -17°.) The angles at C4 are more negative when the bottom half of the water column flows to the equator, as the Doppler shift theory in PB would predict. Conversely, the angles at

C5 are less negative when the currents are flowing equatorward. This is puzzling, for it is not what PB would predict, and the difference is in the sign of the effect, not just the magnitude. Perhaps some alongshore variability in the currents is focusing internal waves. The 20 m current meter at C4 has current ellipses with angles of $\approx$ -60° to the cross-shelf direction with very little scatter with frequency. This anomalous result could be caused by the broken current meter blades found on one of the rotors upon recovery of the mooring.

7. Modal Decomposition

From a modal decomposition of the data, the direction of wave propagation can be found, the vertical structure of the waves can be found and more detailed comparisons can be made to the PB theory. The power in the horizontal and vertical currents can also be shown to be consistent with linearized internal waves. Unfortunately, decomposition into vertical modes can only be done at C4, for the current meters at C5 are badly spaced for a decomposition, and the hourly data at the shallower site make it difficult to compute robust statistics. The details of the decomposition have been left to the appendix, but a summary follows. Using the mean buoyancy profile for the month (Figure 11), the vertical modal structures are calculated for a frequency of 10 cpd, so $f^2 \ll \omega^2 \ll N^2$. These modes, also illustrated in Figure 11, are shown in PB not to vary substantially with frequency for frequencies greater than the critical frequency of reflection and lower than the buoyancy frequency. It is these restrictions that define the 6 to 40 cpd frequency range to which the gathering of statistics is confined. The modes are fit at each time step to the current meter data, with u, v, and w fit independently. The fit is optimal in a least squares sense. The vertical velocity w is determined from the time derivative of temperature and the vertical gradients of temperature.

Figure 11

For this decomposition, only the first two modes are estimated with confidence. These two modes account for 71% of the cross-shore current variance, 50% of the alongshore variance, and 66% of the vertical velocity variance in the frequency range analyzed. Table 2 breaks this down by variable and mode. The angle of the current ellipses and the ellipticity of the current ellipse for the mode 1 wave are shown in Figure 12.

Table 2

Figure 12

The ratio of the power in the horizontal currents to that in the vertical currents for a given mode can be used to check if the high-frequency data are consistent with internal waves. The ratio of the horizontal current power to the vertical current power for a given mode

should be [*Fofonoff*, 1969; PB]

$$\frac{\langle v^2 \rangle + \langle u^2 \rangle}{\langle w^2 \rangle} = \frac{N^2 - \omega_r^2}{\omega_r^2 - f^2} \left(1 + f^2 \omega_r^{-2}\right), \tag{6}$$

for an ocean with a constant N, where ω_r is the frequency of the wave in a frame of reference moving with the barotropic water velocity. PB demonstrates that replacing the constant N with a depth-averaged N makes little difference if $\omega_r^2 \ll N_{\min}^2$, where $N_{\min}$ is the smallest N in the water column, in this case about 50 cpd. The ω_r differs from ω by (PB)

$$\omega_r = \omega - \sin(\theta) V \frac{M\pi}{D} c, \tag{7}$$

where V is the along-shelf barotropic current, M is the mode number, D is the water depth, and θ is the orientation of the internal wave to the cross-shelf direction. V varies with time, and at any given frequency there is an ensemble of waves with varying orientations and amplitudes. In Figure 13 the results for modes 1 and 2 are plotted with the curves predicted by (6) and (7) for $V = \pm 10$ cm s^{-1} and $\theta = \pm 24°$, the latter being the current ellipse angle for mode 1, described below. The data agree well with the curves from (6), especially with the curve in which θ and V are oriented in the same direction, as they are in the data.

Figure 13

The most robust result of the decomposition is that the first mode is dominant at C4. In the cross-shelf velocity the first mode explains 53% of the variance, the second explains 17%. In the along-shelf direction, the numbers are 35% for the first mode and 15% for the second, while in the vertical velocity they are 53% in the first mode and 15% in the second. The lower power in the first-mode alongshore currents compared to the cross-shelf and vertical velocities suggests that waves trapped to the coast are less dominated by the first mode. The higher power in mode 1 is consistent with *Brink* [1988], who predicts that modal internal waves decay at a constant rate per time. Thus, if the waves are coming from the shelf break, those that travel faster will be the least dissipated when they reach a mooring on the shelf. Since second-mode waves have group velocities half as large as first-mode waves, they ought to be and appear to be more attenuated than first-mode waves. Of course, there may have simply been less mode 2 energy entering the shelf from the deep ocean or generated at the shelf break. A more detailed comparison between model and theory is thwarted by a lack of knowledge of the relative strength of the modes at the shelf break.

Because the internal waves at C4 are dominated by the first mode, the top and bottom current meters

should be coherent with each other and incoherent with the middepth current meter. This is the case, and the coherence between the deepest current meter at C4 and a middepth and surface current meter is plotted in Figure 14. The horizontal currents are $\approx 180^\circ$ out of phase between the top and bottom current meters, again consistent with a mode 1 wave (not plotted).

Figure 14

The coherence allows one to investigate the modal structure of the internal waves at a mooring even if the current meters are poorly spaced for a modal decomposition. Figure 14 plots the coherence between the bottommost current meter at the C5 mooring and a middepth and surface current meter. The lack of coherence between the bottom current meter and the surface current meter supports the idea that mode 1 does not dominate at C5 (see section 6.1).

The orientation of the modal current ellipses at C4 is nearly cross isobath, though the orientation changes somewhat with time and mean currents. The depth mean current is equatorward for the first 15 days of July and nearly zero subsequently [*Winant et al.*, 1987]. Nevertheless, the first-mode angle is hardly changed, remaining about -24° as the current changes, while the slower second mode changes its angle from -33° when the bottom current is equatorward to -13° when the current is poleward. This 20° change in angle is comparable to the 10° swing predicted by PB for a 10 cm s^{-1} barotropic current and an isotropic GM spectrum at a 400 m shelf break. In the end, however, the magnitude of the predicted effect of mean current on angle is small, and the uncertainties in the predictions and the data analysis are large. Thus while the second-mode data are not inconsistent with the Doppler shift model in PB, nor are they inconsistent with the simpler model that ignores currents and says that the waves will be perpendicular to the local bathymetry and propagating toward the shore.

PB predicts that the internal wave field propagating in from the shelf break will be focused into a narrow range of angles, and thus the ellipticity of the currents will become independent of frequency and mode. Unfortunately, the predictions of what the ellipticity will be in PB are sensitive to even small amounts of wave energy generated on the shelf. Any waves generated on the shelf can reduce the ellipticity by an order of magnitude if the maximum offshore extent of those waves coincides with the position of the mooring, even if the energy generated on the shelf is much less than the incoming internal waves. The ellipticity of the observed mode 1 waves is about 3.6, while that of the second mode is 2.3, with neither showing an obvious frequency dependence. This

suggests there is relatively more alongshore propagating energy in the second mode than in the first. Also, for both modes the ellipticity increases in the second half of the month, though only in the first mode is this increase significant, from 3.29 to 4.34. This suggests a decrease in alongshore energy in the second part of the month. The tentativeness of this analysis indicates the difficulty of understanding the internal wave field without some measure of the horizontal wave number spectrum.

The modal data can help to determine the direction of internal wave propagation. To do this, it is necessary to define the "spectral correlation coefficient." This is the normalized cospectrum of two time series at a given frequency, defined as

$$\langle vw \rangle = \frac{Co_{vw}}{\sqrt{P_{vv} P_{ww}}}, \tag{8}$$

where Co_{vw} is the cospectrum of v and w and P_{vv} and P_{ww} are the power at a given frequency in v and w, respectively. The structure of an internal wave propagating in the x direction is, when represented modally,

$$u = -\frac{1}{k}\frac{dW}{dz}\sin\left(kx - \omega t + \phi\right), \tag{9a}$$

$$v = \frac{f}{k\omega}\frac{dW}{dz}\cos\left(kx - \omega t + \phi\right), \tag{9b}$$

$$w = W(z)\cos\left(kx - \omega t + \phi\right), \tag{9c}$$

where k is the wave number, ω is the angular frequency, and ϕ is a phase (PB). From (9a)-(9c) it is easy to see that for a single plane wave traveling in the positive x direction, the correlation $\langle vw \rangle$ is 1 and the major axis of the internal wave is oriented along the x axis. Thus, for a single wave, once the angle of the major axis of the current ellipse has been determined for a given frequency, the mean direction of wave propagation along the major axis can be determined from the sign of the correlation of the vertical velocity and the current in the minor axis direction. Unfortunately, for a set of internal waves propagating onto the coast with a range of angles, the computation of the correlation is more complicated. As a simplified version the model in PB, the correlation is calculated assuming waves of equal amplitude and random phase propagating at angles from -θ_c to θ_c around the major axis. Computing the theoretical correlation of the minor axis velocities and the vertical velocities for modally decomposed waves of random phase and constant amplitude, one obtains

$$\langle vw \rangle = \frac{\frac{2f}{\omega}\sin(\theta_c)}{\sqrt{2\theta_c\left(1 + \frac{f^2}{\omega^2}\right) + \theta_c \sin\left(2\theta_c\right)\left(\frac{f^2}{\omega^2} - 1\right)}}, \tag{10}$$

where θ_c is computed in PB as a function of δ, the ratio of the water depth at the observation site to the depth where an internal wave first "feels" the bottom:

$$\theta_c = \arctan\left(\frac{1}{\sqrt{\delta^{-1}-1}}\right). \quad (11)$$

θ_c is shown as a function of δ and $\langle vw \rangle$ is shown as a function of θ_c in Figure 15. Assuming $\delta \approx 0.3$ to 0.4 for the 130 m site, the correlation should lie between 0.1 and 0.4. Correlations of 0.1 to 0.4 for a single frequency are hard to distinguish from white noise. However, it becomes possible to test for propagation onshore if the test is whether the correlation is positive. This test distinguishes waves going onshore from a random wave field, whose correlation would be randomly distributed around zero, and also from waves propagating offshore. It cannot test between various models of the distribution of energy with angle. The test is made by rotating the data at each frequency so that u is in the direction of the major axis that points onshore and v is parallel to the minor axis, which makes the coordinate system right-handed. Then the correlation $\langle vw \rangle$ is formed and plotted in Figure 12. Table 3 gives the percentage of frequencies whose correlation is positive and the confidence that this percentage is distinguishable from an isotropic internal wave field. Since u is rotated so that the onshore component of a positive u is positive, when $\langle vw \rangle$ is positive, the waves are propagating onshore. All of the mode 1 data are consistent with onshore propagation at a better than 93% level, while the mode 2 data are only consistent with onshore propagation before July 15. The mode 2 correlations after July 15 are indistinguishable from white noise.

Figure 15

Table 3

There are some caveats to this method. The correlation is very sensitive to the range of angles over which the waves are propagating. Thus, if an ensemble of waves propagated onshore at a range of angles from -10° to 10° and the same amount of energy went offshore spread between -30° and 30°, this method would indicate that energy was propagating into the shore. These are the limitations of not measuring the wave number spectrum directly.

8. Variation in Power With Space and Time

Inherent in the GM spectrum is an assumption that the energy levels of the internal wave spectrum are constant with time. This is not true for the internal waves on the shelf in the CODE region. The determination that the energy levels are not stationary is tricky, for any finite-length moving average of a truly random time

series will fluctuate. These fluctuations are larger for a red spectrum. Figure 16 is a plot of a 2 day moving average of the power over the 6 to 40 cpd frequency band from the 35, 70, 90, and 121 m current meters at C4, along with 1 standard deviation error bars computed from the periodograms. The error bars account for the redness of the spectrum. The mean energy is also plotted. The standard deviations of the data are small enough and the degrees of freedom large enough, that the chi-square distributions can be considered Gaussian. The observations from 35 m were more than 1 standard deviation from the monthlong mean 32% of the time, at 70 m for 68% of the time, at 90 m for 67% of the time, and at 121 m for 80% of the time. For a stationary Gaussian-distributed time series, this should only be true 34% of the time, indicating that the power levels are not stationary. The variations of the power from the mean power are not more than a factor of 2.5. Very similar results hold for an analysis done over the months of June, July, and August, though the uncertainty in the interpretation increases with the uncertainty in the background stratification over this longer time period.

Figure 16

Neither the fluctuations in N plotted in Figure 4 nor the fluctuations in the along-shelf wind in Figure 17 show any correlation with the power fluctuations. This is also true for the time series of N at the other depths, the time series of winds at other nearby locations, and the time series of alongshore current and current shear. Perhaps the fluctuations in internal wave power are the results of the focusing of internal waves by alongshore variations in the current field.

Figure 17

9. Discussion and Conclusion

The observations can be summarized by contrasting those results that are consistent with internal wave energy existing in the deep ocean as a GM spectrum and propagating onto the shelf and those results that suggest that waves must also be generated, or at least severely modified from the predictions of a linear theory, on the shelf or at the shelf break.

The decline of total energy levels approaching the shore strongly supports the model of waves originating in deep water or at the shelf break and being eroded by friction as they propagate onshore. In a scenario with no friction or any scenario for generation of outward propagating waves near the shore, the energy levels would be expected to increase near the coast.

The orientation and ellipticity of the current ellipses are consistent with an ensemble of internal waves propagating in from the deep ocean, though the failure of the ellipticity to increase shoreward (as predicted by

PB) suggests that waves generated on the shelf are also propagating onshore, thus broadening the angular distribution of the waves. Propagation toward the coast is also supported by the sign of the correlation of the vertical and minor axis velocities of modes 1 and 2 waves.

The dominance of mode 1 waves at the C4 site is again consistent with the frictional model in PB, since mode 1 waves are the least affected by friction. This argument cannot be made more convincing, however, without better knowledge of how deep water modes penetrate onto the shelf. It seems that mode 1 does not dominate at C5.

There are facts that conflict with the picture in PB and indicate that while a GM spectrum propagating in from the deep ocean or shelf break is probably the dominant source of internal waves on the shelf, it is certainly not the only one. It may be that a significant portion of the internal wave energy on the shelf is generated on the shelf. It may also be that the theory is too naive in its linearity, in its simple assumption that the alongshore current is barotropic, or in its assumption of no alongshore variability in topography on frequency.

The most puzzling finding is that the spectrum becomes less red closer to shore. The slower high-frequency waves should be dissipated more rapidly than the low-frequency waves. The observed bluing of the spectrum means that either energy is being generated preferentially at higher frequencies on the shelf or that nonlinear interactions are shifting the energy in the spectrum to the higher frequencies.

Thus the most plausible qualitative synthesis of observations is of a GM spectrum propagating onto the shelf accompanied by shoreward propagating waves generated on the shelf. In order to clarify this possibility, it would be necessary to have observations of the modal structure of the waves at several different locations and ideally some knowledge of the directional spectrum of the waves.

It is also worth observing that on continental shelves broader than at the CODE region, PB indicates that it is likely that dissipation would eliminate all waves from the deep ocean before the shore is reached, which would considerably alter the internal wave climate.

Appendix

In a flat bottom ocean the internal wave spectrum can be broken into vertical modes that are orthogonal to each other [*LeBlond and Mysak*, 1978]. Given u and v as horizontal velocities and w as the vertical velocity,

the linearized system of equations on an f plane is

$$\frac{\partial u}{\partial t} - fv = -\frac{1}{\rho_0}\frac{\partial P}{\partial x}, \quad \text{(A1a)}$$

$$\frac{\partial v}{\partial t} + fu = -\frac{1}{\rho_0}\frac{\partial P}{\partial y}, \quad \text{(A1b)}$$

$$\frac{\partial w}{\partial t} = -\frac{1}{\rho_0}\frac{\partial P}{\partial z} - \frac{\rho g}{\rho_0}, \quad \text{(A1c)}$$

$$\frac{\partial u}{\partial x} + \frac{\partial v}{\partial y} + \frac{\partial w}{\partial z} = 0, \quad \text{(A1d)}$$

$$\frac{\partial \rho}{\partial t} - \frac{\rho_0}{g}N^2(z)w = 0. \quad \text{(A1e)}$$

This system admits internal wave solutions of the form

$$u = -\frac{1}{k}\frac{dW}{dz}\sin\left(kx - \omega t + \phi\right), \quad \text{(A2a)}$$

$$v = \frac{f}{k\omega}\frac{dW}{dz}\cos\left(kx - \omega t + \phi\right), \quad \text{(A2b)}$$

$$w = W(z)\cos\left(kx - \omega t + \phi\right), \quad \text{(A2c)}$$

where ϕ is a phase, k is the horizontal wave number, ω is the angular frequency, and $W(z)$ is the vertical modal structure. $W(z)$ is determined by

$$\frac{d^2W}{dz^2} + k^2\left(\frac{N^2(z) - \omega^2}{\omega^2 - f^2}\right)W = 0 \quad \text{(A3)}$$

with $W = 0$ at the surface and bottom. If N is constant, W has the form

$$W = \sin\left(\frac{M\pi}{D}z\right) \qquad M = 0...\infty. \quad \text{(A4)}$$

If N depends on depth, the structure of the mode is no longer independent of ω^2. However, as shown in PB, if $N^2 \gg \omega^2$, as is true of this analysis, the modal structure is independent of ω^2 to a very good approximation. Thus the modal decomposition will be done for the $\omega = 10$ cpd modes. The results are insensitive to the choice of ω.

This analysis is only true for a flat bottom, however, since the boundary condition is $W = 0$ at the bottom. However, *Wunsch* [1969] showed that the vertical modal solution is approximately valid for waves whose frequencies are much less than the frequency of critical reflection, which is true for this analysis. This approximation is justified in greater detail in PB.

The actual decomposition of the data was done on the horizontal and vertical velocities. The vertical velocities were estimated by assuming the temperature balance

$$T_t + wT_z = 0 \quad \text{(A5)}$$

and computing T_z from low-pass filtered current meter data. The modal functions were computed for the mean hydrography. This is less critical than it may appear, for the low modes are not very sensitive to changes in N. The amplitude of each mode was found by fitting the computed modes to the current meter data at each time record, fitting u, v, and "w" independently. The data were depth weighted, but this made little difference because the current meters were nearly evenly spaced. The fit was optimal in a least squares sense.

This straightforward method obscures several subtle issues in the decomposition. The first problem is that while the internal wave modes are orthogonal, a set of discrete measurements in the water column are not, in general, orthogonal. Unfortunately, to speak meaningfully of power in a mode, that mode must be orthogonal to all others. In order that all of the modes that are fit are nearly orthogonal to each other (in the sense that for two modes $\mathbf{W_1}$ and $\mathbf{W_2}$, $\mathbf{W_1}\cdot\mathbf{W_2}/\sqrt{(\mathbf{W_1}\cdot\mathbf{W_1})(\mathbf{W_2}\cdot\mathbf{W_2})} \ll 1$, where $\mathbf{W_1}\cdot\mathbf{W_2}$ is the inner product of $\mathbf{W_1}$ and $\mathbf{W_2}$ evaluated at the measurement points), only five modes can be fit to the seven current meters. The fit is judged successful because the sum of the power in each mode and the residual (as shown in Table 2) is never more than 6% different from the total power. If the data from the top two current meters are discarded, the power in the modes explains 180% of the variance, with most of the duplication of power being in the lowest two modes. Thus discarding the top two current meters is untenable.

It is unfortunate that the need for orthogonality forces one to use the top two current meters, since they are on a different mooring. This mooring is described as nominally being 100 m to the northwest of the subsurface mooring and was certainly not more than 200 m away [*Beardsley et al.*, 1985, and S. J. Lentz, personal communication 1997]. The horizontal decorrelation length scale for horizontal currents will be half a wavelength for waves with a finite beam width.

Figure A1 is a plot of the wavelengths of the first five modes as a function of frequency. From this it can be seen that if the separation between the first two moorings is 100 m, mode 2 becomes nearly decorrelated at 40 cycles per day. In the worst case, with a separation of 200 m, the second mode becomes decorrelated at about 23 cycles per day.

Figure A1

The amount of power in a real mode that is spuriously transferred to another mode because of any decorrelation of the top 2 m from the lower current meters can be calculated. This calculation shows that, at the worst case of 200 m separation, 20% of mode 1 horizontal cur-

rent power will leak into mode 2, while 20% of the horizontal current power in mode 2 can leak into mode 1. However, only 5% percent of the vertical current power in mode 2 can leak into mode 1 vertical current power and vice versa. Little mode 1 and 2 power would be leaked to the higher modes. The vertical power is 53% in the first mode and 15% in the second mode, and the cross-shore power is 53% in the first mode and 17% in the second (Table 2). This partition remains true for frequencies in the 25-40 cpd range. If the two moorings were so far apart that mode 1 would decorrelate, the cross-shore mode 2 power would be greater than the vertical mode 2 power, since more of the horizontal mode 1 power would leak into horizontal mode 2 than vertical mode 1 power into vertical mode 2. Likewise, if only mode 2 decorrelated, the fraction of cross-shore power in mode 2 would be less than the fraction of vertical power in mode 2, since more mode 2 power would leak in the horizontal modes than vertical modes. Thus the the moorings are probably 100 m or less apart.

Even with only 100 m between the two current meter moorings, it must be assumed that modes higher than the second are decorrelated. Similar calculations to the ones above show that it becomes impossible to sort out the energy in the higher but resolvable modes but that the partition of about 30% of the energy to modes higher than the second mode is robust.

The possibility of modes higher than the theoretically observable fifth mode being aliased into the low modes is impossible to rule out, but it seems improbable that it is significant because the energy decreases monotonically for the first five modes.

Acknowledgments. I would like to thank the people who helped me get the data for this paper, especially Susan Tarbell and Carol Alessi, both of whom helped me find the current meter data and tutored me in the interpretation of mooring logs. The data came from the CODE programs, and so thanks go to all who collected the data and planned the programs. This paper benefited greatly from Steve Lentz's close reading and would have been impossible without Ken Brink's many readings and numerous pieces of scientific advice. The work was funded by an Office of Naval Research fellowship and Office of Naval Research AASERT fellowship, N00014-95-1-0746. Woods Hole Oceanographic Institution contribution 9629.

References

Beardsley, R. C., and S. J. Lentz, The Coastal Ocean Dynamics Experiment collection: An introduction, *J. Geophys. Res.*, *92(C2)*, 1455–1463, 1987.

Beardsley, R. C., R. Limeburner, and L. K. Rosenfeld, Introduction, in CODE-2: Moored Array and Large-Scale Data Report, *Technical Report 85-35*, Woods Hole Oceanogr. Inst., Woods Hole, Mass., Nov. 1985.

Brink, K. H., On the effect of bottom friction on internal waves, *Cont. Shelf Res.*, *8(*4), 397–403, 1988.

Fofonoff, N. P., Spectral characteristics of internal waves in the ocean, *Deep Sea Res.*, *16*, 59–71, 1969.

Garrett, C., and W. Munk, Space-time scales of internal waves, *Geophys. Fluid Dyn.*, *3*, 225–264, 1972.

Gordon, R. L., Internal wave climate near the coast of northwest Africa during JOINT-1, *Deep Sea Res.*, *25*, 625–643, 1978.

Howell, T. L., and W. S. Brown, Nonlinear internal waves on the california continental shelf, *J. Geophys. Res.*, *90(C4)*, 7256–7264, 1985.

Huyer, A., J. Fleischbein, and R. Schramm, Hydrographic data from the second coastal ocean dynamics experiment: R/V Wecoma, Leg 9, 6-27 July 1982, *Data Report 109, Ref. 84-7*, Coll. of Oceanogr., Oregon State Univ., Corvallis, April, 1983.

Kosro, P. M., and A. Huyer, CTD and velocity surveys of seaward jets off northern California, July 1981 and 1982, *J. Geophys. Res.*, *91(C6)*, 7680–7690, 1986.

Kunze, E., Near-inertial wave propagation in geostrophic shear, *J. Phys. Oceanogr.*, *15*, 544–565, 1985.

LeBlond, P. H., and L. A. Mysak, *Waves in the Ocean*, Elsevier Sci., New York, 1978.

Lighthill, J., *Waves in Fluids*, Cambridge Univ. Press, New York, 1978.

Lynch, J. F., G. Jin, R. Pawlowicz, D. Ray, C. -S. Chiu, J. H. Miller, R. H. Bourke, A. R. Parsons, and R. Muench, Acoustic travel-time perturbations due to shallow-water internal waves and internal tides in the Barents Sea Polar Front: Theory and experiment, *J. Acoust. Soc. of Am.*, *99(2)*, 289–297, 1996.

McKee, W. D., Internal-inertial waves in a fluid of variable depth, *Proc. Cambridge Philos. Soc.*, *73*, 205–213, 1973.

Pringle, J. M., and K. H. Brink, High Frequency Internal Waves on a Sloping Shelf, *J. Geophys. Res.*, this issue.

Sandstrom, H., and J. A. Elliott, Internal tide and solitons on the scotian shelf: A nutrient pump at work, *J. Geophys. Res.*, *89(C4)*, 6415–6426, 1984.

Sanford, L. P., and W. D. Grant, Dissipation of internal wave energy in the bottom noundary layer on the continental shelf, *J. Geophys. Res.*, *92(C*2), 1828–1844, 1987.

Winant, C. D., R. C. Beardsley, and R. E. Davis, Moored wind, temperature, and current observations made during coastal ocean dynamics experiments 1 and 2 over the northern california continental shelf and upper slope, *J. Geophys. Res.*, *92(C2)*, 1569–1604, 1987.

Wunsch, C., Geographical variability of the internal wave feild: A search for sources and sinks, *J. Phys. Oceanogr.*, *6*, 471–485, 1976.

Wunsch, C., On the propagation of internal waves up a slope, *Deep Sea Res.*, *15*, 251–258, 1968.

Wunsch, C., Progressive internal waves on slopes, *J. Fluid Mech.*, *35*, 131–144, 1969.

James Pringle, Scripps Institution of Oceanography, Univerisity of California, San Diego, Mail Stop 0218, La Jolla, CA 92093-0218 (email: pringle@alum.mit.edu)

(Received July 18, 1997; revised July 28, 1998;
accepted August 14, 1998.)

---

[1]Now at Scripps Institution of Oceanography, University of California, San Diego, La Jolla.

Paper number 1998JC900053.
0148-0227/98/1998JC900053$09.00

(Received July 18, 1997; revised July 28, 1998;
accepted August 14, 1998.)

Copyright 1999 by the American Geophysical Union.

Paper number 1998JC900053.
0148-0227/98/1998JC900053$09.00

Table 1. Angle That the Average Current Ellipse Makes With the Cross-Shore Direction and the Ellipticity of the Current Ellipse for the C4 and C5 Moorings for the 2 Week Periods Before and After July 15, 1982

	Before July 15		After July 15	
Depth, m	Mean Angle, deg	Ellipticity	Mean Angle,deg	Ellipticity
		C4 Mooring		
10	-36±6	2.49±0.37	-23±5	2.79±0.42
20	-72±7	1.83±0.39	-49±4	2.83±0.28
35	-16±53*	1.35±0.21*	-49±21	1.60±0.40
55	-22±9	1.64±0.25	-17±18	1.53±0.23
70	-20±15	1.83±0.38	-2±9	1.95±0.36
90	-12±16	1.53±0.25	4±9	2.03±0.35
121	-16±5	4.41±1.17	-16±4	5.02±0.80
		C5 Mooring		
20	-4±27	1.34±0.16*	-15±15	1.91±0.34
35	-8±24	1.37±0.22	-10±10	2.00±0.54
55	-17±5	1.79±0.31	-26±5	2.35±0.38
70	-9±9	2.27±0.47	-13±3	2.42±0.39
90	-13±11	1.93±0.27	-9±6	2.49±0.31
110	-20±7	2.31±0.43	-22±7	3.21±0.62
150	-12±6	2.81±0.69	-20±10	2.06±0.63
250	-26±37	1.53±0.33	-34±21	1.47±0.31
350	-14±7	2.73±0.79	-22±8	2.62±0.68

The averages are made by calculating the ellipticity and angle at each frequency in the 6 to 40 cpd frequency range and then averaging the results with an even weighting. The deviations are standard deviation, not the standard error.

Stars mark ellipticity or angles not significantly different from white noise at the 95% confidence level, using the tests described in the text.

Table 2. Percent Variance Explained by Mode for the Modal Decomposition

Mode	Alongshore Velocity	Cross-shore Velocity	Vertical Velocity
1	35	53	53
2	15	17	15
3/barotropic	11	4	10
Residual	32	27	22
Total variance	94	101	100

Values are in percent. The third mode for the horizontal velocities is the barotropic mode, not the real third mode. It is fit to reduce the crossing of any barotropic mode into the first and second modes. The total variance does not sum to 100% because the three discretely sampled modes are neither orthogonal nor complete. Details are in the appendix.

Table 3. Percentages of Frequency Bins Whose Vertical Velocity Versus Minor Axis Velocity Correlation is Greater Than Zero.

	Mode 1	Confidence	Mode 2	Confidence
Before July 15	100	>95	71	93
After July 15	71	93	45	none

Values are in percent. For waves traveling onshore this should be 100%; for an isotropic wave field it should be 50%. The confidence level is the confidence that it is the former, not the latter.

Figure 1. The Coastal Ocean Dynamics Experiment (CODE) region, showing the central line of moorings from the CODE II experiment. The C5, C4, and C3 moorings are used herein.

Figure 1. The Coastal Ocean Dynamics Experiment (CODE) region, showing the central line of moorings from the CODE II experiment. The C5, C4, and C3 moorings are used herein.

Figure 2. (top) Hydrography for the CODE region for the April-July upwelling regime and (bottom) standard deviations.

Figure 2. (top) Hydrography for the CODE region for the April-July upwelling regime and (bottom) standard deviations.

Figure 3. Average buoyancy frequency found from conductivity-temperature-depth (CTD) casts on the shelf and shelf break in July 1982. The thick line is the value computed with a full equation of state, while the thin line uses the empirical relation between temperature and potential density given by (5). The data have been smoothed by a 10 m boxcar average.

Figure 3. Average buoyancy frequency found from conductivity-temperature-depth (CTD) casts on the shelf and shelf break in July 1982. The thick line is the value computed with a full equation of state, while the thin line uses the empirical relation between temperature and potential density given by (5). The data have been smoothed by a 10 m boxcar average.

Figure 4. Buoyancy frequency of water between 55 and 70 m at C4 as a function of time. The data were low-pass filtered with a filter that had a half-amplitude pass at 3.25 times the inertial period (f=1.24 cpd) and a full pass at 4 times the inertial period.

Figure 4. Buoyancy frequency of water between 55 and 70 m at C4 as a function of time. The data were low-pass filtered with a filter that had a half-amplitude pass at 3.25 times the inertial period (f=1.24 cpd) and a full pass at 4 times the inertial period.

Figure 5. Low-pass-filtered alongshore currents at (top to bottom) 35 m depth at C3; 20 m depth at C4; 90 m depth at C4; and 110 m depth at C5. The same low-pass filter was used as in Figure 4.

Figure 5. Low-pass-filtered alongshore currents at (top to bottom) 35 m depth at C3; 20 m depth at C4; 90 m depth at C4; and 110 m depth at C5. The same low-pass filter was used as in Figure 4.

Figure 6. Power spectra of cross- and along-shelf velocity for current meters (top) C5 at 90 m depth, (middle) C4, 90 m depth, and (bottom) C3, 70 m depth. The thin solid line is the cross-shore power, the dashed line is the alongshore power, and the thick solid line is the *Garrett and Munk* [1972] power. The stars on the frequency axis mark the limits of the frequency range analyzed. The power is in $cm^2\ s^{-1}$, frequency is in cycles per day.

Figure 6. Power spectra of cross- and along-shelf velocity for current meters (top) C5 at 90 m depth, (middle) C4, 90 m depth, and (bottom) C3, 70 m depth. The thin solid line is the cross-shore power, the dashed line is the alongshore power, and the thick solid line is the *Garrett and Munk* [1972] power. The stars on the frequency axis mark the limits of the frequency range analyzed. The power is in $cm^2\ s^{-1}$, frequency is in cycles per day.

Figure 7. Power in the 6 - 40 cpd frequency band normalized by the *Garrett and Munk* [1972] spectrum for (top) C5 and (bottom) C4 moorings.

Figure 7. Power in the 6 - 40 cpd frequency band normalized by the *Garrett and Munk* [1972] spectrum for (top) C5 and (bottom) C4 moorings.

Figure 8. Slope of the power spectrum of each current meter in log-log space from (top) C5 and (bottom) C4.

Figure 8. Slope of the power spectrum of each current meter in log-log space from (top) C5 and (bottom) C4.

Figure 9. Major axis of the illustrated current ellipse (thick line), and the angle of the major axis to the cross-shore direction θ, which is positive as drawn.

Figure 9. Major axis of the illustrated current ellipse (thick line), and the angle of the major axis to the cross-shore direction θ, which is positive as drawn.

Figure 10. (top) Power spectra and (bottom) the angle that the major axis of the current meter makes with the cross-shelf direction for the (left) first and (right) last half of July for the current meter in 55 m of water at the C5 mooring. The arrows on the bottom axis mark the frequency limits of the analysis.

Figure 10. (top) Power spectra and (bottom) the angle that the major axis of the current meter makes with the cross-shelf direction for the (left) first and (right) last half of July for the current meter in 55 m of water at the C5 mooring. The arrows on the bottom axis mark the frequency limits of the analysis.

Figure 11. (left) Horizontal velocity structure of the first three modes and (right) buoyancy frequency profile. The stars on the vertical axis mark the position of the current meters at C4.

Figure 11. (left) Horizontal velocity structure of the first three modes and (right) buoyancy frequency profile. The stars on the vertical axis mark the position of the current meters at C4.

Figure 12. (top) Angle of the current ellipses, (middle) ellipticity of the current ellipse, and (bottom) correlation between the currents parallel to the minor axis of the ellipse and the vertical velocity for mode 1. The stars on the horizontal axis mark the frequency limit of analysis.

Figure 12. (top) Angle of the current ellipses, (middle) ellipticity of the current ellipse, and (bottom) correlation between the currents parallel to the minor axis of the ellipse and the vertical velocity for mode 1. The stars on the horizontal axis mark the frequency limit of analysis.

Figure 13. Ratio of the horizontal and vertical current powers for (top) mode 1, and (bottom) mode 2. The solid line is the solution to (6) when the along-shelf barotropic velocity $V = 0$ and/or the orientation of the internal wave to the cross-shelf direction $\theta = 0$, while the dashed lines are for $V = \pm 10$ cm s^{-1} and $\theta = \pm 24°$. The lower curve is for when the sign of V and θ differ, the upper curve is for when they are of the same sign. The error bars on the data are $\pm$ 1 standard deviation.

Figure 13. Ratio of the horizontal and vertical current powers for (top) mode 1, and (bottom) mode 2. The solid line is the solution to (6) when the along-shelf barotropic velocity $V = 0$ and/or the orientation of the internal wave to the cross-shelf direction $\theta = 0$, while the dashed lines are for $V = \pm 10$ cm s^{-1} and $\theta = \pm 24°$. The lower curve is for when the sign of V and θ differ, the upper curve is for when they are of the same sign. The error bars on the data are $\pm$ 1 standard deviation.

Figure 14. Coherence of cross-shelf current between the bottommost current meter and the surface and middepth current meters for the C4 and C5 moorings. The thick line is the 95% confidence level.

Figure 14. Coherence of cross-shelf current between the bottommost current meter and the surface and middepth current meters for the C4 and C5 moorings. The thick line is the 95% confidence level.

Figure 15. (top) Correlation between the vertical velocity and the horizontal velocity parallel to the minor axis as a function of angular beam width and wave frequency. (bottom) Beam width as a function of the ratio of depth at which the waves feel the bottom to the depth of the current meter.

Figure 15. (top) Correlation between the vertical velocity and the horizontal velocity parallel to the minor axis as a function of angular beam width and wave frequency. (bottom) Beam width as a function of the ratio of depth at which the waves feel the bottom to the depth of the current meter.

Figure 16. The 2 day moving average of the power from the (top to bottom) 20, 70, 90, and 121 m current meters at the 130 m site, along with 1 standard deviation error bars. The mean power is plotted as the thick horizontal line.

Figure 16. The 2 day moving average of the power from the (top to bottom) 20, 70, 90, and 121 m current meters at the 130 m site, along with 1 standard deviation error bars. The mean power is plotted as the thick horizontal line.

Figure 17. The alongshelf winds at C4 for the month of July. The winds have been low-pass filtered with the same filter as used for Figures 4 and 5.

Figure 17. The alongshelf winds at C4 for the month of July. The winds have been low-pass filtered with the same filter as used for Figures 4 and 5.

Figure A1. Wavelengths of the first three internal wave modes in 130 m of water as a function of frequency; $N = 77$ cpd.

Figure A1. Wavelengths of the first three internal wave modes in 130 m of water as a function of frequency; $N = 77$ cpd.

Please have AGU resize this figure

Figure 1

Please have AGU resize this figure

Figure 2

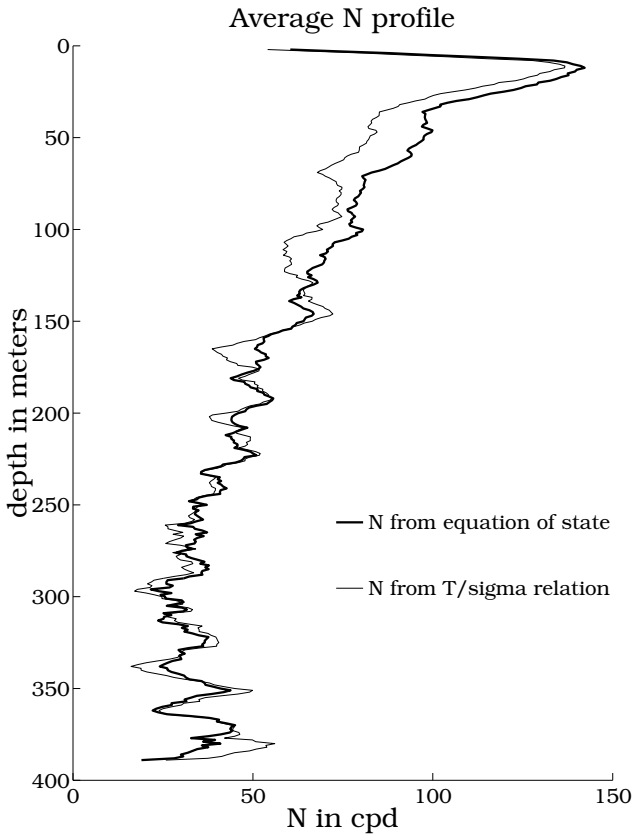
Average N profile
depth in meters
N in cpd
N from equation of state
N from T/sigma relation
0
50
100
150
200
250
300
350
400
0
50
100
150

Figure 3

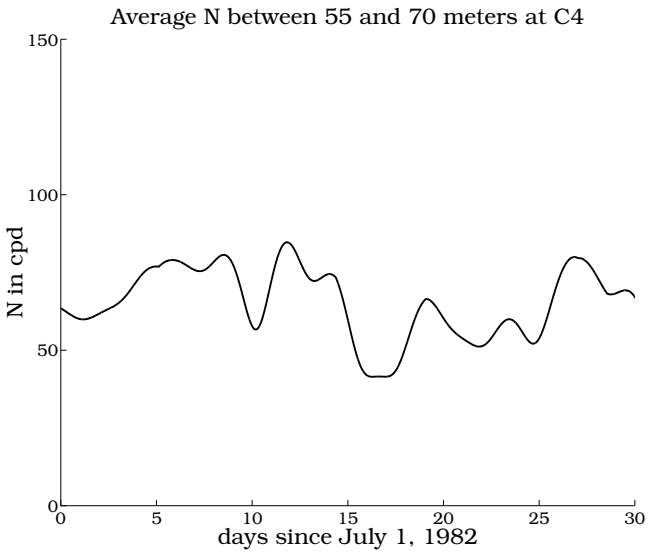
Average N between 55 and 70 meters at C4
150
100
50
0
N in cpd
0
5
10
15
20
25
30
days since July 1, 1982

Figure 4

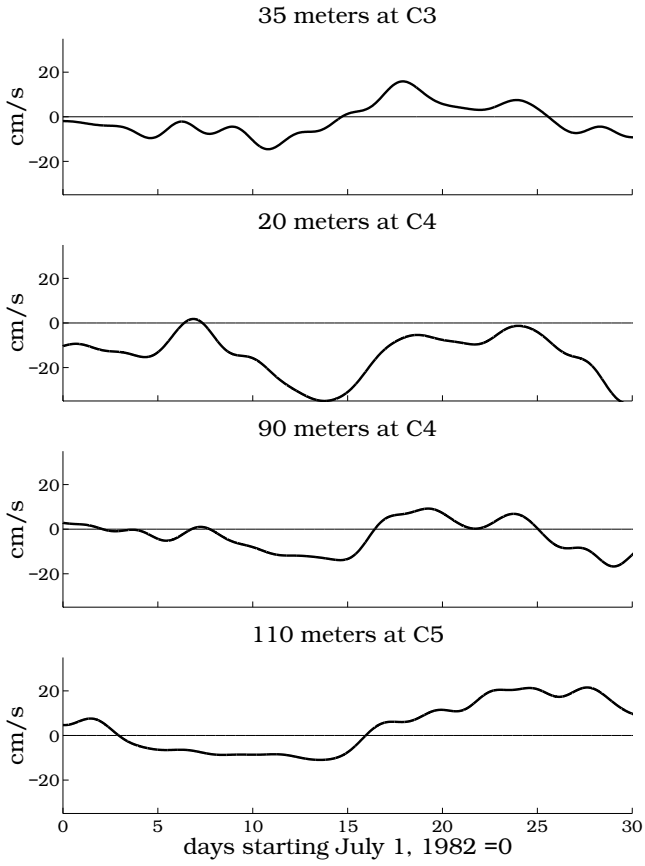
35 meters at C3
20 meters at C4
90 meters at C4
110 meters at C5
cm/s
20
0
−20
0
5
10
15
20
25
30
days starting July 1, 1982 =0

Figure 5

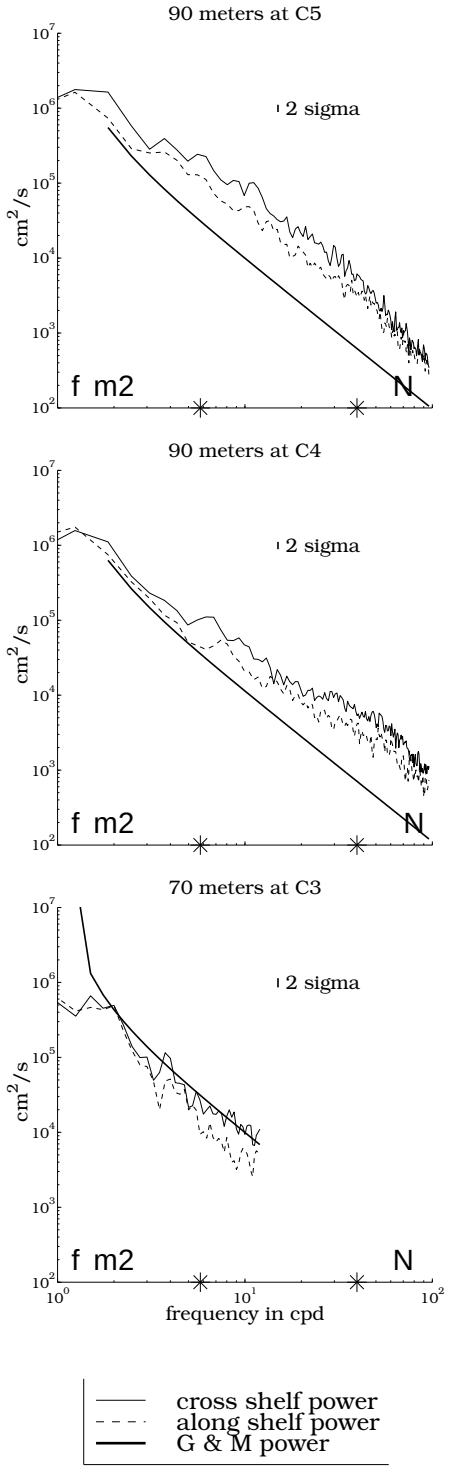
90 meters at C5
2 sigma
cm^2/s
f m2
N
90 meters at C4
2 sigma
cm^2/s
f m2
N
70 meters at C3
2 sigma
cm^2/s
f m2
N
frequency in cpd
cross shelf power
along shelf power
G & M power

Figure 6

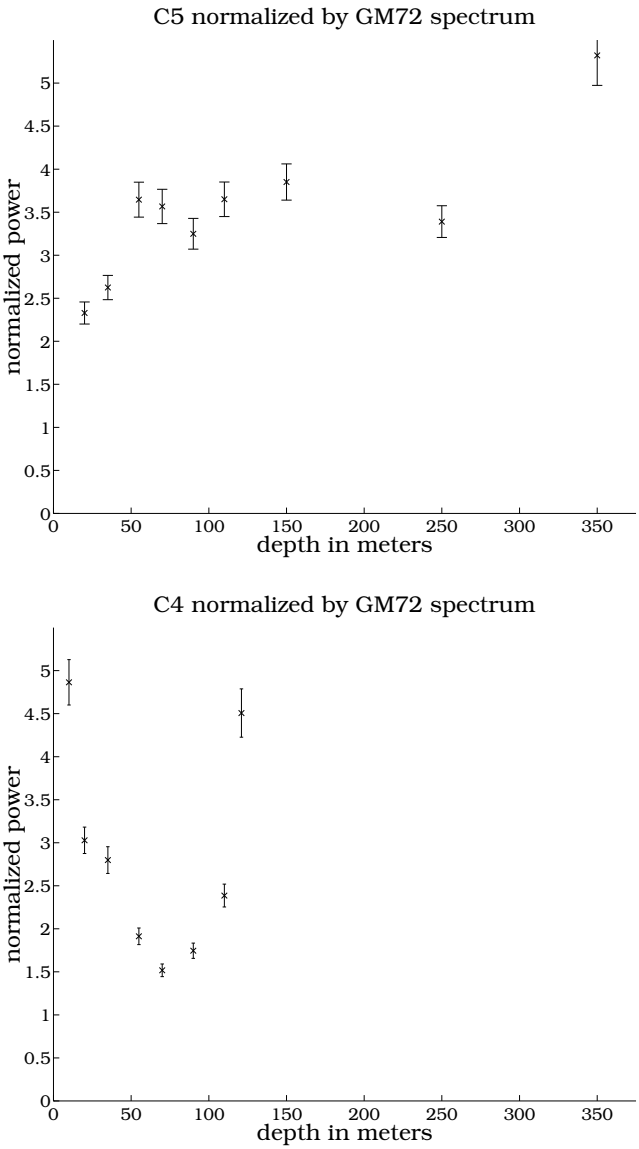
C5 normalized by GM72 spectrum
normalized power
depth in meters
C4 normalized by GM72 spectrum
normalized power
depth in meters

Figure 7

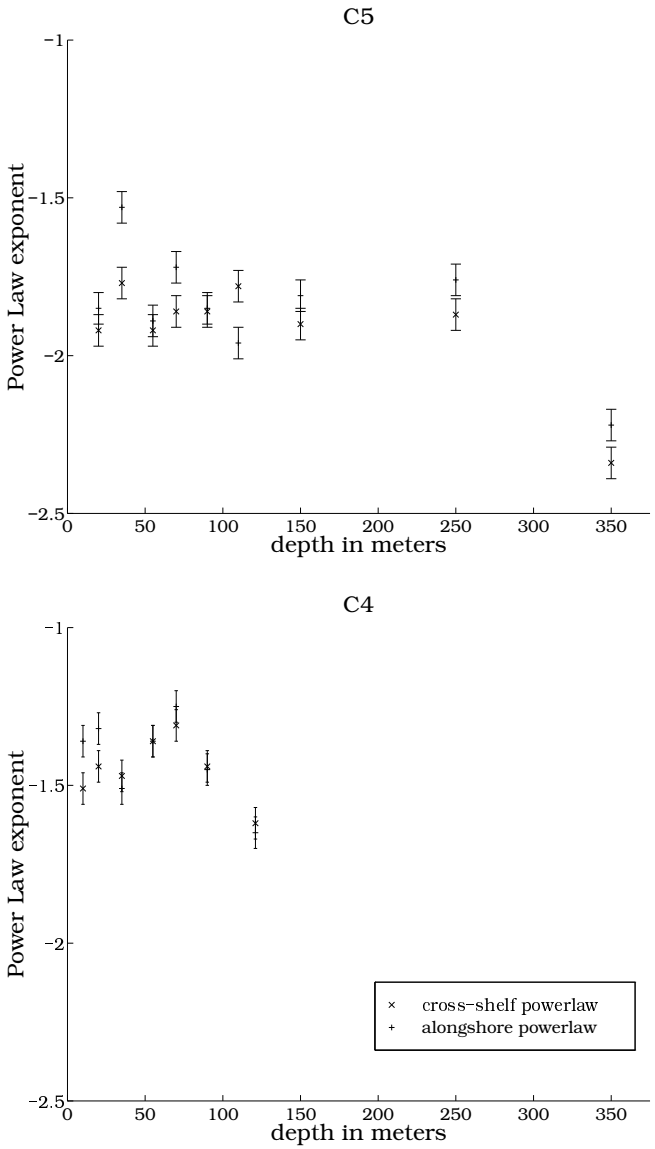
C5
Power Law exponent
depth in meters
C4
Power Law exponent
depth in meters
cross−shelf powerlaw
alongshore powerlaw

Figure 8

definition of current ellipse angle

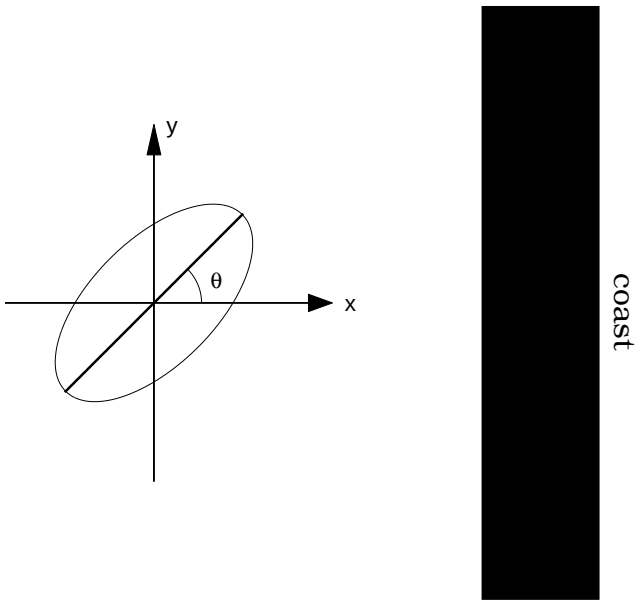

Figure 9

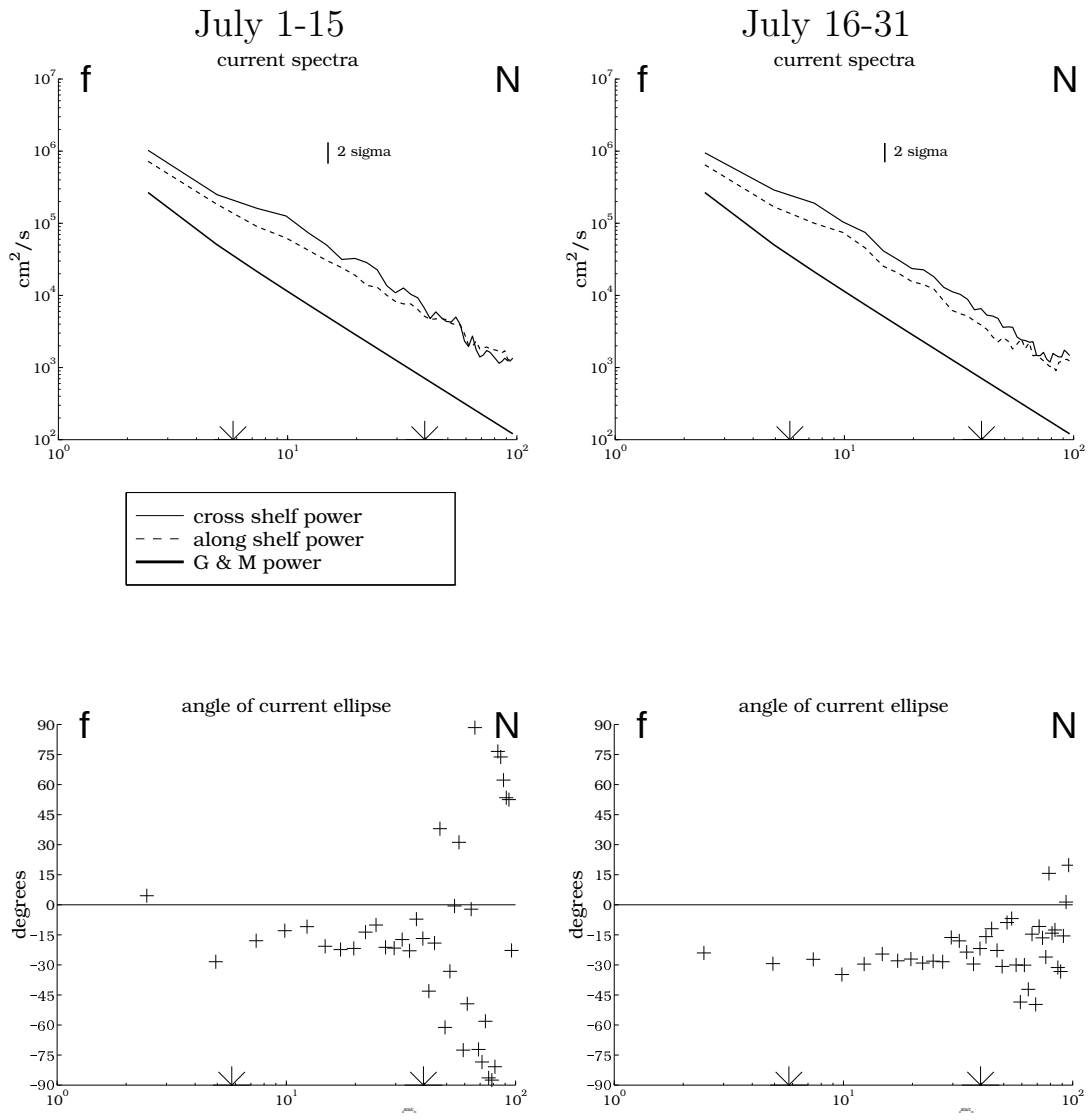
July 1-15
current spectra
f
N
2 sigma
cm²/s
July 16-31
current spectra
f
N
2 sigma
cm²/s
cross shelf power
along shelf power
G & M power
angle of current ellipse
f
N
degrees
angle of current ellipse
f
N
degrees

Figure 10

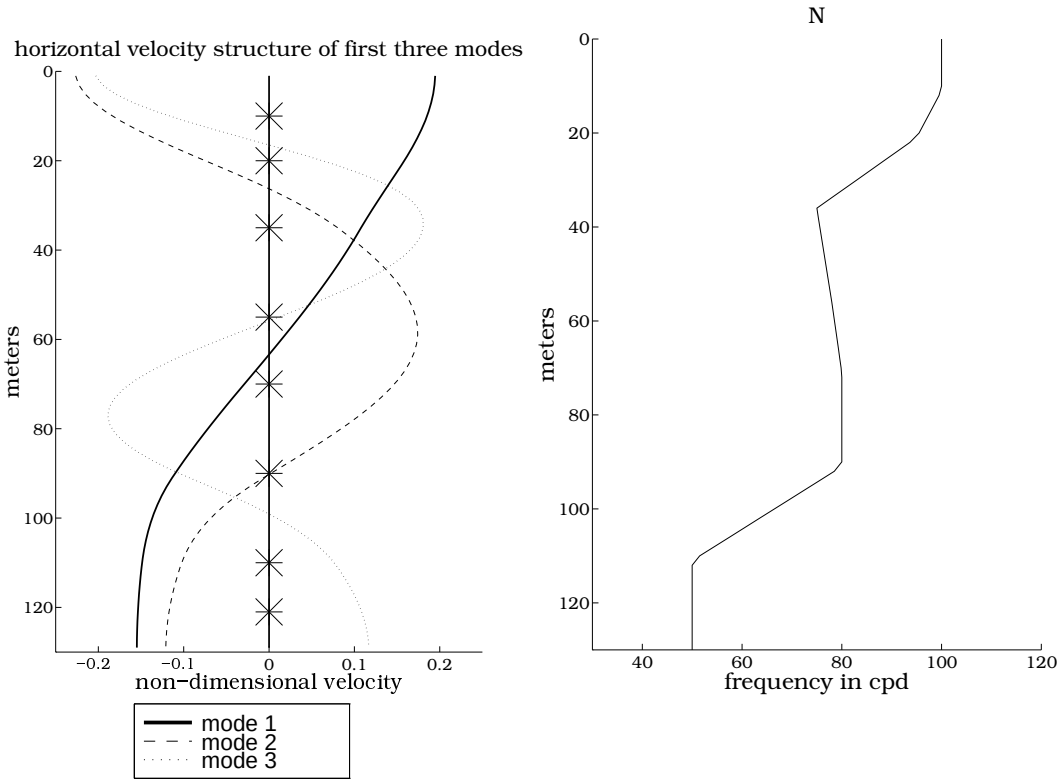
horizontal velocity structure of first three modes
meters
0
20
40
60
80
100
120
−0.2
−0.1
0
0.1
0.2
non−dimensional velocity
mode 1
mode 2
mode 3
N
meters
0
20
40
60
80
100
120
40
60
80
100
120
frequency in cpd

Figure 11

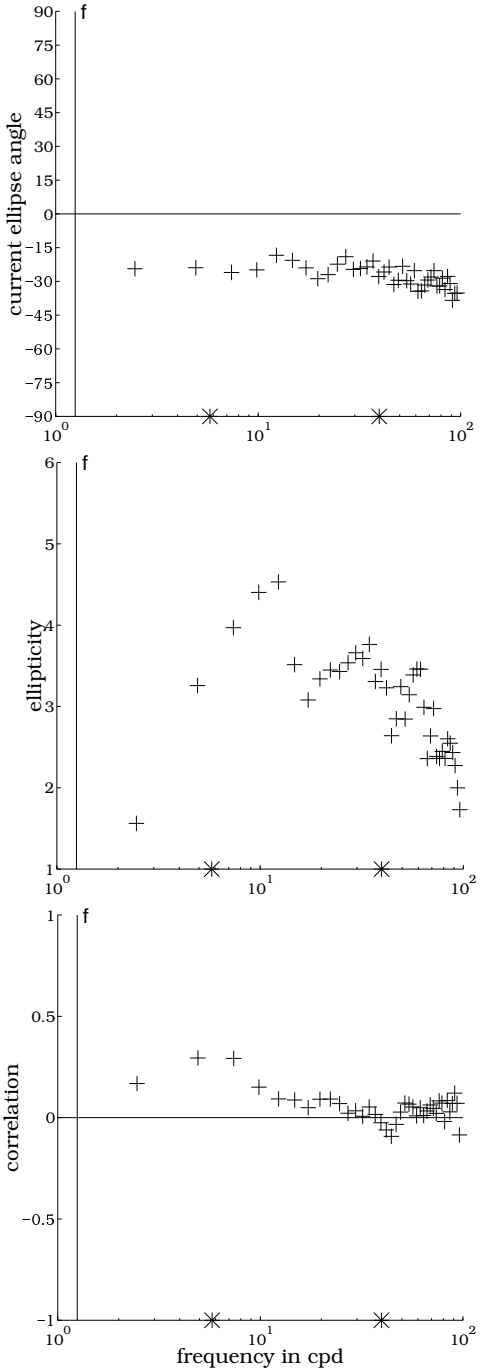
f
current ellipse angle
90
75
60
45
30
15
0
−15
−30
−45
−60
−75
−90
10^0
10^1
10^2
f
ellipticity
6
5
4
3
2
1
10^0
10^1
10^2
f
correlation
1
0.5
0
−0.5
−1
10^0
10^1
10^2
frequency in cpd

Figure 12

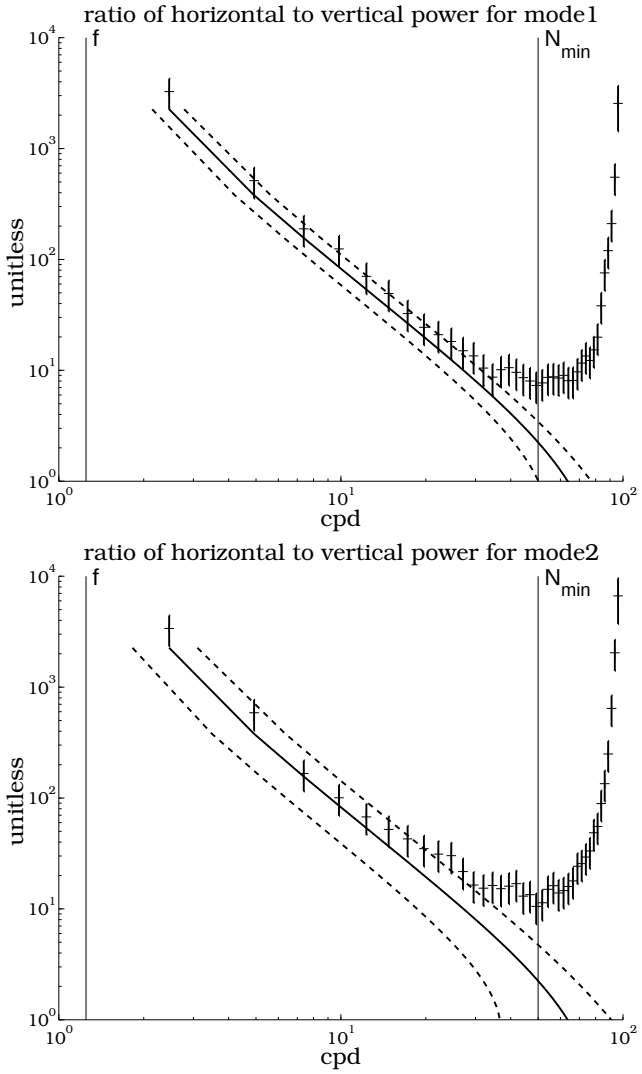
ratio of horizontal to vertical power for mode1
f
N_min
unitless
cpd
ratio of horizontal to vertical power for mode2
f
N_min
unitless
cpd

Figure 13

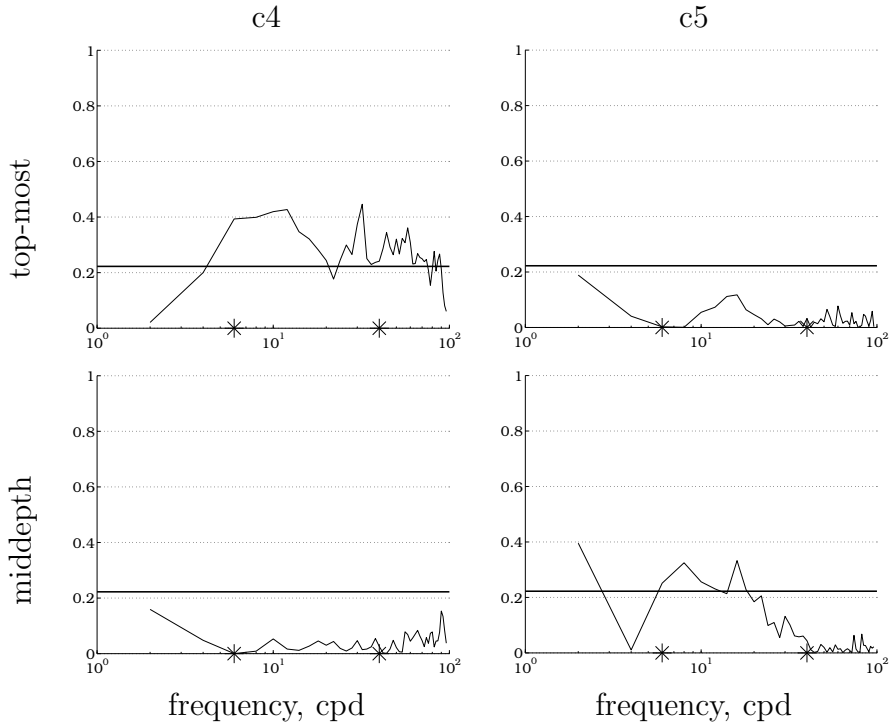

Figure 14

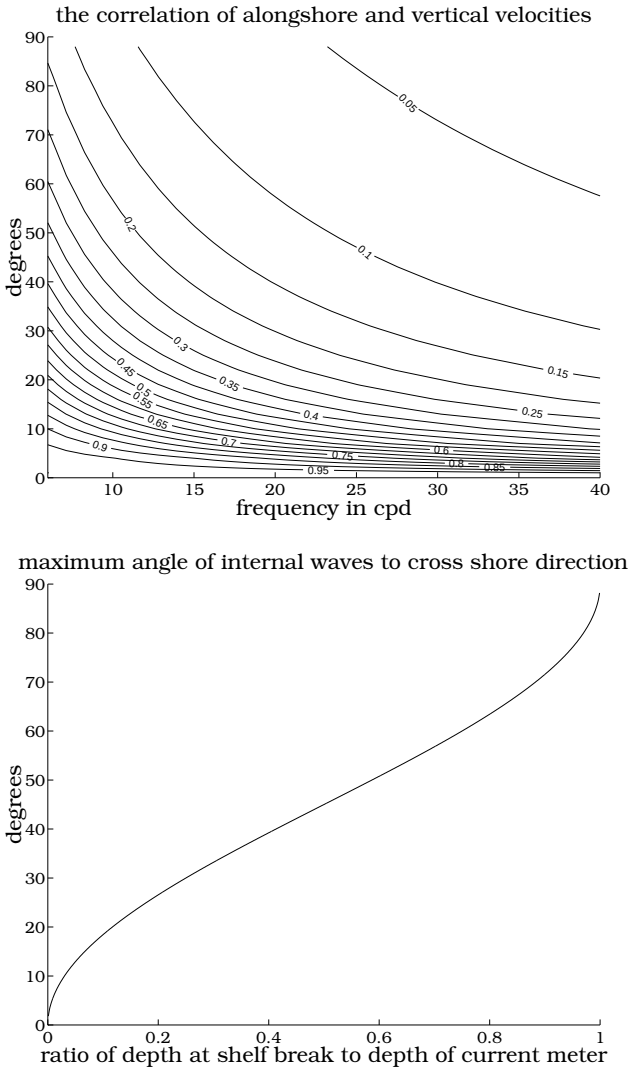
the correlation of alongshore and vertical velocities
degrees
frequency in cpd
0.05
0.1
0.15
0.2
0.25
0.3
0.35
0.4
0.45
0.5
0.55
0.6
0.65
0.7
0.75
0.8
0.85
0.9
0.95
maximum angle of internal waves to cross shore direction
degrees
ratio of depth at shelf break to depth of current meter

Figure 15

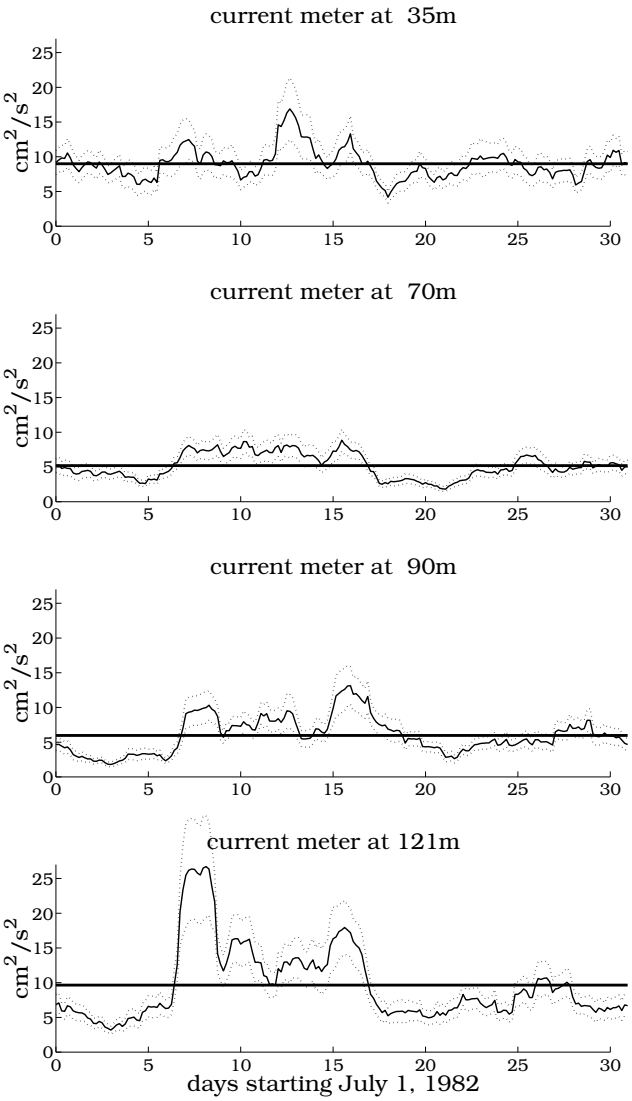
current meter at 35m
current meter at 70m
current meter at 90m
current meter at 121m
cm^2/s^2
0
5
10
15
20
25
30
days starting July 1, 1982

Figure 16

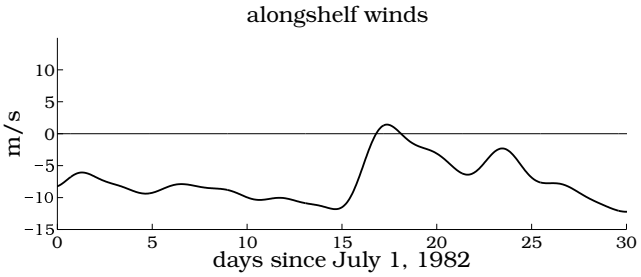
alongshelf winds
m/s
10
5
0
−5
−10
−15
0
5
10
15
20
25
30
days since July 1, 1982

Figure 17

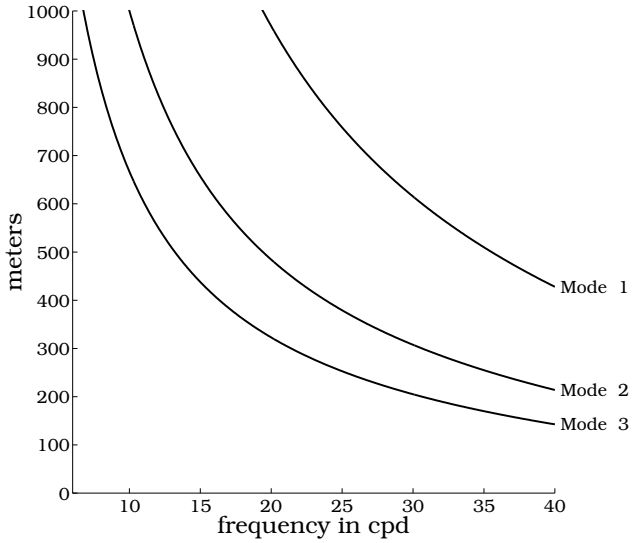

Figure A1

PRINGLE: OBSERVATIONS OF HIGH-FREQUENCY INTERNAL WAVES

PRINGLE: OBSERVATIONS OF HIGH-FREQUENCY INTERNAL WAVES

PRINGLE: OBSERVATIONS OF HIGH-FREQUENCY INTERNAL WAVES

PRINGLE: OBSERVATIONS OF HIGH-FREQUENCY INTERNAL WAVES

PRINGLE: OBSERVATIONS OF HIGH-FREQUENCY INTERNAL WAVES

PRINGLE: OBSERVATIONS OF HIGH-FREQUENCY INTERNAL WAVES

PRINGLE: OBSERVATIONS OF HIGH-FREQUENCY INTERNAL WAVES

PRINGLE: OBSERVATIONS OF HIGH-FREQUENCY INTERNAL WAVES

PRINGLE: OBSERVATIONS OF HIGH-FREQUENCY INTERNAL WAVES

PRINGLE: OBSERVATIONS OF HIGH-FREQUENCY INTERNAL WAVES

PRINGLE: OBSERVATIONS OF HIGH-FREQUENCY INTERNAL WAVES

PRINGLE: OBSERVATIONS OF HIGH-FREQUENCY INTERNAL WAVES

PRINGLE: OBSERVATIONS OF HIGH-FREQUENCY INTERNAL WAVES

PRINGLE: OBSERVATIONS OF HIGH-FREQUENCY INTERNAL WAVES

PRINGLE: OBSERVATIONS OF HIGH-FREQUENCY INTERNAL WAVES

PRINGLE: OBSERVATIONS OF HIGH-FREQUENCY INTERNAL WAVES

PRINGLE: OBSERVATIONS OF HIGH-FREQUENCY INTERNAL WAVES

PRINGLE: OBSERVATIONS OF HIGH-FREQUENCY INTERNAL WAVES

PRINGLE: OBSERVATIONS OF HIGH-FREQUENCY INTERNAL WAVES

PRINGLE: OBSERVATIONS OF HIGH-FREQUENCY INTERNAL WAVES

PRINGLE: OBSERVATIONS OF HIGH-FREQUENCY INTERNAL WAVES

PRINGLE: OBSERVATIONS OF HIGH-FREQUENCY INTERNAL WAVES

PRINGLE: OBSERVATIONS OF HIGH-FREQUENCY INTERNAL WAVES

PRINGLE: OBSERVATIONS OF HIGH-FREQUENCY INTERNAL WAVES

PRINGLE: OBSERVATIONS OF HIGH-FREQUENCY INTERNAL WAVES

PRINGLE: OBSERVATIONS OF HIGH-FREQUENCY INTERNAL WAVES

PRINGLE: OBSERVATIONS OF HIGH-FREQUENCY INTERNAL WAVES

PRINGLE: OBSERVATIONS OF HIGH-FREQUENCY INTERNAL WAVES

PRINGLE: OBSERVATIONS OF HIGH-FREQUENCY INTERNAL WAVES

PRINGLE: OBSERVATIONS OF HIGH-FREQUENCY INTERNAL WAVES

PRINGLE: OBSERVATIONS OF HIGH-FREQUENCY INTERNAL WAVES

PRINGLE: OBSERVATIONS OF HIGH-FREQUENCY INTERNAL WAVES

PRINGLE: OBSERVATIONS OF HIGH-FREQUENCY INTERNAL WAVES

PRINGLE: OBSERVATIONS OF HIGH-FREQUENCY INTERNAL WAVES

PRINGLE: OBSERVATIONS OF HIGH-FREQUENCY INTERNAL WAVES

PRINGLE: OBSERVATIONS OF HIGH-FREQUENCY INTERNAL WAVES

PRINGLE: OBSERVATIONS OF HIGH-FREQUENCY INTERNAL WAVES

PRINGLE: OBSERVATIONS OF HIGH-FREQUENCY INTERNAL WAVES

PRINGLE: OBSERVATIONS OF HIGH-FREQUENCY INTERNAL WAVES

PRINGLE: OBSERVATIONS OF HIGH-FREQUENCY INTERNAL WAVES

PRINGLE: OBSERVATIONS OF HIGH-FREQUENCY INTERNAL WAVES

PRINGLE: OBSERVATIONS OF HIGH-FREQUENCY INTERNAL WAVES

PRINGLE: OBSERVATIONS OF HIGH-FREQUENCY INTERNAL WAVES

PRINGLE: OBSERVATIONS OF HIGH-FREQUENCY INTERNAL WAVES

PRINGLE: OBSERVATIONS OF HIGH-FREQUENCY INTERNAL WAVES

PRINGLE: OBSERVATIONS OF HIGH-FREQUENCY INTERNAL WAVES

PRINGLE: OBSERVATIONS OF HIGH-FREQUENCY INTERNAL WAVES

PRINGLE: OBSERVATIONS OF HIGH-FREQUENCY INTERNAL WAVES

PRINGLE: OBSERVATIONS OF HIGH-FREQUENCY INTERNAL WAVES

PRINGLE: OBSERVATIONS OF HIGH-FREQUENCY INTERNAL WAVES

PRINGLE: OBSERVATIONS OF HIGH-FREQUENCY INTERNAL WAVES

PRINGLE: OBSERVATIONS OF HIGH-FREQUENCY INTERNAL WAVES

PRINGLE: OBSERVATIONS OF HIGH-FREQUENCY INTERNAL WAVES

PRINGLE: OBSERVATIONS OF HIGH-FREQUENCY INTERNAL WAVES

PRINGLE: OBSERVATIONS OF HIGH-FREQUENCY INTERNAL WAVES

PRINGLE: OBSERVATIONS OF HIGH-FREQUENCY INTERNAL WAVES

PRINGLE: OBSERVATIONS OF HIGH-FREQUENCY INTERNAL WAVES

PRINGLE: OBSERVATIONS OF HIGH-FREQUENCY INTERNAL WAVES

PRINGLE: OBSERVATIONS OF HIGH-FREQUENCY INTERNAL WAVES

PRINGLE: OBSERVATIONS OF HIGH-FREQUENCY INTERNAL WAVES

PRINGLE: OBSERVATIONS OF HIGH-FREQUENCY INTERNAL WAVES

PRINGLE: OBSERVATIONS OF HIGH-FREQUENCY INTERNAL WAVES

PRINGLE: OBSERVATIONS OF HIGH-FREQUENCY INTERNAL WAVES

PRINGLE: OBSERVATIONS OF HIGH-FREQUENCY INTERNAL WAVES

PRINGLE: OBSERVATIONS OF HIGH-FREQUENCY INTERNAL WAVES

PRINGLE: OBSERVATIONS OF HIGH-FREQUENCY INTERNAL WAVES

PRINGLE: OBSERVATIONS OF HIGH-FREQUENCY INTERNAL WAVES

PRINGLE: OBSERVATIONS OF HIGH-FREQUENCY INTERNAL WAVES

PRINGLE: OBSERVATIONS OF HIGH-FREQUENCY INTERNAL WAVES

PRINGLE: OBSERVATIONS OF HIGH-FREQUENCY INTERNAL WAVES

PRINGLE: OBSERVATIONS OF HIGH-FREQUENCY INTERNAL WAVES

PRINGLE: OBSERVATIONS OF HIGH-FREQUENCY INTERNAL WAVES

PRINGLE: OBSERVATIONS OF HIGH-FREQUENCY INTERNAL WAVES

PRINGLE: OBSERVATIONS OF HIGH-FREQUENCY INTERNAL WAVES

PRINGLE: OBSERVATIONS OF HIGH-FREQUENCY INTERNAL WAVES

PRINGLE: OBSERVATIONS OF HIGH-FREQUENCY INTERNAL WAVES

PRINGLE: OBSERVATIONS OF HIGH-FREQUENCY INTERNAL WAVES

PRINGLE: OBSERVATIONS OF HIGH-FREQUENCY INTERNAL WAVES

PRINGLE: OBSERVATIONS OF HIGH-FREQUENCY INTERNAL WAVES

PRINGLE: OBSERVATIONS OF HIGH-FREQUENCY INTERNAL WAVES

PRINGLE: OBSERVATIONS OF HIGH-FREQUENCY INTERNAL WAVES

PRINGLE: OBSERVATIONS OF HIGH-FREQUENCY INTERNAL WAVES

PRINGLE: OBSERVATIONS OF HIGH-FREQUENCY INTERNAL WAVES

PRINGLE: OBSERVATIONS OF HIGH-FREQUENCY INTERNAL WAVES

PRINGLE: OBSERVATIONS OF HIGH-FREQUENCY INTERNAL WAVES

PRINGLE: OBSERVATIONS OF HIGH-FREQUENCY INTERNAL WAVES

PRINGLE: OBSERVATIONS OF HIGH-FREQUENCY INTERNAL WAVES

PRINGLE: OBSERVATIONS OF HIGH-FREQUENCY INTERNAL WAVES

PRINGLE: OBSERVATIONS OF HIGH-FREQUENCY INTERNAL WAVES

PRINGLE: OBSERVATIONS OF HIGH-FREQUENCY INTERNAL WAVES

53

PRINGLE: OBSERVATIONS OF HIGH-FREQUENCY INTERNAL WAVES

PRINGLE: OBSERVATIONS OF HIGH-FREQUENCY INTERNAL WAVES

PRINGLE: OBSERVATIONS OF HIGH-FREQUENCY INTERNAL WAVES

PRINGLE: OBSERVATIONS OF HIGH-FREQUENCY INTERNAL WAVES

PRINGLE: OBSERVATIONS OF HIGH-FREQUENCY INTERNAL WAVES

PRINGLE: OBSERVATIONS OF HIGH-FREQUENCY INTERNAL WAVES

PRINGLE: OBSERVATIONS OF HIGH-FREQUENCY INTERNAL WAVES